Published in final edited form as:

*Nat Immunol*. 2022 June ; 23(6): 904–915. doi:10.1038/s41590-022-01213-2.

# Cytotoxic Innate Lymphoid Cells Sense Cancer Cell-Expressed Interleukin-15 to Suppress Human and Murine Malignancies

**Emily R. Kansler**[1,2,‡],

**Saïda Dadi**[1,‡],

**Chirag Krishna**[3],

**Briana G. Nixon**[1,4],

**Efstathios G. Stamatiades**[1],

**Ming Liu**[1],

**Fengshen Kuo**[5],

**Jing Zhang**[1],

**Xian Zhang**[1],

**Kristelle Capistrano**[1],

**Kyle A. Blum**[5],

**Kate Weiss**[5],

**Ross M. Kedl**[6],

**Guangwei Cui**[7],

**Koichi Ikuta**[7],

**Timothy A. Chan**[5],

**Christina S. Leslie**[3],

**A. Ari Hakimi**[8,†],

**Ming O. Li**[1,2,4,†,*]

[1]Immunology Program, Memorial Sloan Kettering Cancer Center, New York, NY 10065, USA

[2]Louis V. Gerstner Jr. Graduate School of Biomedical Sciences, Memorial Sloan Kettering Cancer Center, New York, NY, 10065, USA

[*]Correspondence: lim@mskcc.org.

[‡]These authors contributed equally

[†]These authors jointly supervised this work

AUTHOR CONTRIBUTIONS:

M.O.L., S.D., and E.R.K. conceived the project. E.R.K. performed and analyzed most experiments with input from M.O.L and A.A.H. Bioinformatics and data analysis were conducted by C.K. and F.K. with input from C.S.L and T.A.C. E.S.G. performed the immunofluorescence and intravital imaging experiments. B.G.N. generated *Gzmc*$^{tdT\text{-}T2A\text{-}iCre}$ mice and assisted with the design and execution of experiments with human tissue. J.Z. and H.Z. characterized the mouse models. M.L discovered differential innate lymphocyte and CD8$^{+}$ T cell responses in chRCC and ccRCC patients, and made major contributions in generating the bulk RNA-seq dataset. K.A.B. and K.W. assisted with collection of human tissues. K.J.C. helped manage the mouse colony. R.M.K provided the IL-15$^{2A\text{-}eGFP}$ reporter mouse. K.I. and G. C. provided the *Il15*$^{fl}$ mouse. E.R.K. wrote and M.O.L. edited the manuscript.

COMPETING INTERESTS:

MSKCC has filed a patent application with the U.S. Patent and Trademark Office directed toward targeting ILC1 IL-15 signaling for cancer immunotherapy. M.O.L is an SAB member of and holds equity or stock options in Amberstone Biosciences Inc and META Pharmaceuticals Inc. The remaining authors declare no competing interests.

[3]Computational and Systems Biology Program, Memorial Sloan Kettering Cancer Center, New York, NY, 10065, USA

[4]Immunology and Microbial Pathogenesis Graduate Program, Weill Cornell Graduate School of Medical Sciences, Cornell University, New York, NY, 10065, USA

[5]Human Oncology and Pathogenesis Program, Memorial Sloan Kettering Cancer Center, New York, NY, 10065, USA

[6]Department of Immunology and Microbiology, University of Colorado Anschutz Medical Campus, Aurora, CO, 80045, USA

[7]Laboratory of Immune Regulation, Department of Virus Research, Institute for Frontier Life and Medical Sciences, Kyoto University, Kyoto, 606-8507, Japan

[8]Department of Urology, Memorial Sloan Kettering Cancer Center, New York, NY, 10065, USA

## Abstract

Malignancy can be suppressed by the immune system. However, the classes of immunosurveillance responses and their mode of tumor sensing remain incompletely understood. Here, we show that while clear cell renal cell carcinoma (ccRCC) was infiltrated by exhaustion-phenotype $CD8^+$ T cells which negatively correlated with patient prognosis, chromophobe RCC had abundant infiltration of granzyme A-expressing intraepithelial type 1 innate lymphoid cells (ILC1s) that positively associated with patient survival. Interleukin-15 (IL-15) promoted ILC1 granzyme A expression and cytotoxicity, and IL-15 expression in chRCC tumor tissue positively tracked with the ILC1 response. An ILC1 gene signature also predicted survival of a subset of breast cancer patients in association with IL-15 expression. Notably, ILC1s directly interacted with cancer cells, and IL-15 produced by cancer cells supported the expansion and anti-tumor function of ILC1s in a murine breast cancer model. Thus, ILC1 sensing of cancer cell IL-15 defines an immunosurveillance mechanism of epithelial malignancies.

## INTRODUCTION:

The theory of cancer immunosurveillance originally attributed the protective mechanisms to adaptive immune responses, in particular antigen-specific lymphocytes[1]. Studies since then have demonstrated that T cells can indeed play a critical role in restraining tumor growth in carcinogen-induced or virally associated cancers, especially those in which the process of carcinogenesis results in immunogenic antigen expression[2]. However, activation by tumor antigens generally results in robust regulatory mechanisms that restrain T cell responses, most notably through engagement of inhibitory checkpoint receptors such as programmed cell death protein 1 (PD-1). The clinical success of immunotherapy approaches that remove these brakes have produced durable responses in some cancer subtypes including clear cell renal cell carcinoma (ccRCC)[3, 4].

However, many tumor types lack expression of immunogenic antigens[2]. Of note, innate lymphocytes can mediate cancer immunosurveillance with natural killer (NK) cells being the most studied particularly in hematological malignancies[5]. In addition to circulating NK cells, reports over the last decade have revealed heterogeneous populations of innate

lymphocytes to include tissue-resident innate lymphoid cells (ILCs) that are generally not considered to be cytotoxic[6]. Nonetheless, type 1 ILCs (ILC1s) can exert NK cell-like cytolytic activities[7, 8, 9], and expand in models of epithelial cancer[7]. But, how they are able to sense and detect cancer cells is not yet clear. In humans, CD56 is used as a marker of innate lymphocytes classically defined as NK cells, generally subset into $CD56^{bright}$ and $CD56^{dim}$ populations that are abundant in tissues and circulation, respectively[10]. As ILCs can express CD56, the identity of CD56-expressing innate lymphocytes in healthy or cancerous tissues remains poorly defined[11]. Of note, the transcription factor Hobit, encoded by *Zfp683* in mice and *ZNF683* in humans, has been shown to be an ILC1 lineage marker and a driver of ILC1 tissue residency and effector programs[8, 12, 13, 14].

In this study, we set forth to investigate tumor-elicited cytotoxic lymphocyte responses in human RCC patients. We found that while ccRCC tumors were predominantly infiltrated with $CD8^+$ T cells, chromophobe RCC (chRCC) tumors had abundant infiltration of tissue-resident $CD56^{bright}$ innate lymphocytes, phenotypically similar to ILC1s, that expressed high levels of Hobit and the cytotoxic molecule granzyme A. The cytokine interleukin-15 (IL-15) induced granzyme A expression and promoted the cytotoxic function of tumor-resident ILC1s. Moreover, a gene expression signature of ILC1s correlated with IL-15 expression in chRCC tumors as well as in breast tumors harboring gain-of-function mutations of *PIK3CA*, and predicted patient survival. Utilizing a murine model of breast cancer, we further discovered that cancer cell-expressed IL-15 was essential for the expansion, effector differentiation, and anti-tumor function of ILC1s. These findings demonstrate that induction of ILC1s represents an innate anti-tumor immune response of epithelial cancers with immunosurveillance outcome tuned towards the sensing of cancer cell-expressed IL-15.

## RESULTS:

### ccRCC tumors are abundantly infiltrated by $PD1^+CD8^+$ T cells

RCC is among the top 10 most common cancers in both men and women with histologically distinct subtypes manifesting differential responses to therapies[15]. Notably, while immune checkpoint blockade therapy has significantly increased survival of ccRCC patients, chRCC patients are generally refractory to the treatment[16]. To define the immunological basis of this differential outcome, we performed single-cell RNA sequencing on $CD45^+$ cells isolated from late-stage tumors of ccRCC and chRCC patients. Pooled data revealed 10 major clusters defined by lineage marker plots and differential gene expression analysis (Fig. 1a, Extended Data Fig. 1a, and Supplementary Table 1). Of note, the overall abundance of the different immune cell clusters was markedly different between the two cancer subtypes (Fig. 1b). Among the three $CD8^+$ T cell clusters, cluster CD8_1 and clusters CD8_2A and 2B contained cells mostly from chRCC and ccRCC patients, respectively (Fig. 1c). Notably, cluster CD8_1 had a gene expression profile marked by high expression of *S1PR5* and *KLF2* (Fig. 1d, Extended Data Fig. 1b, and Supplementary Table 1), molecules implicated in mediating cell egress into the blood and lymphatic system[17]. Clusters CD8_2A and 2B showed highly similar gene expression profiles and expressed T cell exhaustion markers *PDCD1* and *TOX* (Fig. 1d, Extended Data Fig. 1b, and Supplementary Table 1),

but clustered separately based on differences in the expression of immediate early genes including *FOSB* and *NR4A1* (Fig. 1d, Extended Data Fig. 1b, and Supplementary Table 1).

We then sought to substantiate these findings and thus performed flow cytometric analyses on an extensive cohort of RCC patient tumor, tumor-adjacent normal kidney, and blood samples. We observed that ccRCC tumors had significantly more $CD8^+$ T cells compared to adjacent normal kidney and blood, reflecting either infiltration or expansion in the tumor, while chRCC patients had no significant difference in $CD8^+$ T cell abundance across tissues (Fig. 1e and Extended Data Fig. 1c). In addition, quantification of PD-1 expression revealed that higher percentages of $CD8^+$ T cells from ccRCC tumors expressed PD-1 than their normal kidney and blood counterparts (Fig. 1f). With rare exception, chRCC $CD8^+$ T cells were practically PD-1-negative across tissues suggesting that like the $CD8^+$ T cells profiled by single-cell RNA sequencing in the chRCC patient, these cells were bystanders not engaged in active surveillance (Fig. 1f). Overall, these data suggest that contrary to ccRCC patients, chRCC patients generally do not have a conventional PD-$1^+CD8^+$ T cell response in tumors.

## chRCC tumors are highly enriched for ILC1s

In addition to three clusters of $CD8^+$ T cells, two clusters of innate lymphocytes defined by high expression of *KLRB1* encoding the killer cell lectin-like receptor CD161 were detected by single-cell RNA sequencing (Fig. 1a and Extended Data Fig. 2a). Their phenotypes were distinct in terms of expression of surface molecules and transcription factors with one cluster, like cluster CD8_1, expressing high levels of *S1PR5* and *KLF2* that define circulating NK cells[18] (Fig. 2a, Extended Data Fig. 2a, and Supplementary Table 1). The other cluster expressed high levels of *ITGA1* encoding the integrin CD49a, and *ZNF683* which encodes the transcription factor Hobit that defines tissue-resident ILC1s[18] (Fig. 2a, Extended Data Fig. 2a, and Supplementary Table 1). Both NK and ILC1 clusters were present in each histology, but cluster ILC1was more abundant in chRCC than ccRCC (Fig. 2b). Both clusters displayed potential for cytotoxicity, but had differences in granzyme expression, such as *GZMH* and *GZMA* expressed in cluster NK and cluster ILC1, respectively (Extended Data Fig. 2a and Supplementary Table 1). These data suggest that two distinct populations of innate lymphocytes with cytotoxic potential exist in RCC tumors – one predominantly circulating with canonical NK cell features and the other tissue-resident with ILC1 properties.

To confirm these findings, we analyzed an extensive RCC patient cohort by flow cytometry. There was a significant increase in total $CD3^-CD56^+$ innate lymphocytes in chRCC, but not ccRCC, tumors compared to adjacent normal kidney and blood (Fig. 2c and Extended Data Fig. 2b). We probed the $CD3^-CD56^+$ population for ILC1s and NK cells by expression of CD49a and CD103, another integrin molecule that promotes lymphocyte retention in epithelial cancer[19]. Notably, the vast majority of $CD3^-CD56^+$ cells in the blood and adjacent normal kidney were $CD49a^-CD103^-$ NK-phenotype cells (Fig. 2d). In contrast, there was a substantial increase in $CD49a^+CD103^+$ ILC1s in tumor tissues of both histologies, however the magnitude of the response was significantly higher in chRCC compared to ccRCC (Fig. 2d). To further characterize these two innate lymphocyte populations in RCC tumors, we

measured the level of CD56 expression and noted that the $CD49a^{+}CD103^{+}$ ILC1 population consistently expressed higher levels of CD56 than the $CD49a^{-}CD103^{-}$ NK cell subset in chRCC, but not ccRCC, tumors (Extended Data Fig. 2c). Together, these findings reveal that chRCC tumors are characterized by robust expansion and activation of ILC1s.

## ILC1 response predicts better overall survival in chRCC

Thus far our data demonstrate that ccRCC tumors are populated by exhausted $CD8^{+}$ T cells and ILC1s, while chRCC tumors are populated by only the latter. To explore the functional relevance of these tumor-elicited responses, we generated signatures of the $CD8^{+}$ T cell and ILC1 clusters. Given the overall similarities of clusters CD8_2A and CD8_2B, we combined them into one cluster and performed pairwise differential gene expression (DEG) analysis relative to every other $CD45^{+}$ cluster retrieved from single-cell RNA sequencing (Supplementary Table 1). The resulting gene set included genes significantly upregulated in CD8_2A and CD8_2B in every comparison, and included the exhaustion markers *PDCD1*, *LAG3*, and *TOX* (Fig. 3a and Supplementary Table 1). Application of the CD8_2 gene signature to the ccRCC and chRCC TCGA cohorts showed a negative association of enrichment of this signature and overall survival for both histologies (Fig. 3b) in line with a recent study[20], likely a reflection of an ineffectual $CD8^{+}$ T cell response that tracks with disease progression.

Similarly, we generated a gene signature for the ILC1 cluster by performing pairwise DEG analysis relative to every other cluster to obtain a set of significantly upregulated genes in the ILC1 cluster in every comparison (Fig. 3c and Supplementary Table 1). To further validate the ILC1 gene signature, we applied it to an independent cohort of 69 bulk RNA sequencing datasets of immune cell as well as non-immune cell populations isolated from ccRCC and chRCC patient tumors (Extended Data Fig. 3a). For a total of 12 individual ILC1 samples and 57 non-ILC1 cell populations, the signature was highly discriminative for ILC1s as indicated by the high areas under both receiver operating characteristic (ROC) and precision recall (PR) curves (Extended Data Fig. 3). Interestingly, high expression of the ILC1 gene signature was associated with better and worse overall survival in chRCC and ccRCC patients, respectively (Fig. 3d). Of note, all chRCC patients that fell in the top quartile for ILC1 gene signature expression had a 100% survival rate (Fig. 3d), suggesting the potential for a prognostic marker as well as a mechanism of effective tumor control.

The opposing predictive values of the ILC1 gene signature on ccRCC and chRCC patients' survival suggested phenotypic and functional heterogeneity of ILC1s. A potentially functional ILC1 signature gene was *GZMA* (Fig. 3c), which encodes a cytotoxic molecule involved in lytic granule-mediated noncanonical apoptosis and pyroptosis[21, 22]. Examination of granzyme A protein expression among a cohort of chRCC and ccRCC patients revealed that ILC1s consistently expressed more granzyme A than matched NK cell counterparts, but only in chRCC tumors (Fig. 4a). In fact, ILC1s had lower granzyme A expression than NK cells in most ccRCC tumors (Fig. 4a). In addition, ILC1s from tumor tissue expressed higher levels of granzyme A than ILC1s from adjacent normal kidney, again more consistently in chRCC patients (Fig. 4b). Thus, despite induction of ILC1s in both chRCC

and ccRCC tumors, they exhibit disparate patterns of granzyme A expression in association with histology-specific prognosis of the ILC1 gene signature.

## IL-15 promotes ILC1 expansion and function in chRCC

We wished to define how ILC1 responses were differentially regulated in RCC tumors. The ILC1 cluster was enriched for the *KLRC1* transcript (Extended Data Fig. 4a), which encodes for the inhibitory receptor NKG2A. Flow cytometry experiments revealed that compared to NK cells, ILC1s from both chRCC and ccRCC tumors had a higher fraction of cells expressing NKG2A as well as higher levels of NKG2A protein expression (Extended Data Fig. 4b). To determine whether differential exposure of ILC1s to the NKG2A ligand HLA-E might affect ILC1 responses in RCC, we examined *HLAE* transcript expression in the TCGA database, and observed lower *HLAE* expression in chRCC tumors than ccRCC tumors (Extended Data Fig. 4c). Nonetheless, *HLAE* expression was not anti-correlated with ILC1 signature in chRCC tumors (Extended Data Fig. 4d), nor did it negatively track with chRCC patient survival (Extended Data Fig. 4e). These observations suggest that NKG2A sensing of HLA-E is unlikely a major determinant of the ILC1 response in RCC.

The cytokine IL-15 in complex with IL-15 receptor α chain (IL-15Rα) promotes the development, maintenance, and effector function of lymphocytes with cytotoxic potential. Previous studies have shown that brief priming with IL-15 markedly enhances the antitumor response of $CD56^{bright}$ NK cells isolated from blood[23]. Thus, we explored whether IL-15 played a role in the regulation of ILC1s. Indeed, both the NK and ILC1 clusters from single-cell RNA sequencing data showed high expression of *IL2RB* (Extended Data Fig. 5a), encoding the shared signaling IL-2/IL-15 receptor β chain. Notably, chRCC tumors from the TCGA cohort had higher expression of *IL15* transcripts than ccRCC tumors (Extended Data Fig. 5b), implying that the level of IL-15 in the tumor microenvironment may regulate tissue-resident innate lymphocyte responses in a dose-dependent manner.

To explore the potential role of IL-15 in control of ILC1 function, we isolated these cells from RCC tumors and cultured them with two different doses of an IL-15/IL-15Rα complex, 10 and 100 ng/ml. The higher dose of IL-15/IL-15Rα complex induced greater expression of granzyme A and CD56 (Fig. 4c and Extended Data Fig. 5c), two proteins enriched in chRCC ILC1s (Fig. 4a and Extended Data Fig. 2c). In addition, the higher dose of IL-15/IL-15Rα substantially enhanced the cytotoxicity of ILC1s against target cells in a single-cell killing assay (Fig. 4d). The higher dose of IL-15/IL-15Rα also resulted in increased expression of the cell proliferation marker Ki67 (Fig. 4e), in agreement with greater expansion of ILC1s in chRCC than ccRCC tumors (Fig. 2d). Of note, there was a positive correlation of level of IL-15 expression and enrichment of the ILC1 signature across the chRCC TCGA patient cohort (Fig. 4f). Moreover, patients with higher expression of IL-15 trended towards better overall survival than patients with lower expression (Fig. 4g). Collectively, these findings demonstrate that IL-15 regulates the cytotoxic program of tissue-resident ILC1s and enhances their ability to kill target cells, which may represent a critical mechanism for tumor control in chRCC patients.

### ILC1 expansion tracks with IL-15 expression in breast cancer

We next sought to explore whether IL-15 governs the ILC1-mediated cancer immunosurveillance in other epithelial malignancies. As the most common cancer worldwide, breast cancer composes of heterogenous subsets defined by immunohistochemical and genomic markers[24]. Phenotypic profiling of mammary tumors revealed differential cell surface protein expression in tumor-infiltrating type 1 innate lymphocytes, including high expression of the ILC1-enriched NKG2A inhibitory receptor[25]. Although these cells were broadly classified as "NK cells"[25], they could represent ILC1s as ILCs including Hobit-expressing ILC1s are abundant in mammary tumors revealed by a recent single-cell RNA sequencing study[26]. To probe the function and regulation of ILC1s in breast cancer, we applied the ILC1 gene signature to the TCGA database and found that patients with higher ILC1 signature trended to have better survival at earlier time points (Fig. 5a), although it did not reach statistical significance. However, the ILC1 signature predicted better survival of patients that harbor the hotspot *PIK3CA* mutations (p.H1047R, p.E545K, or p.E542K) (Fig. 5b), and the ILC1 signature value positively tracked with *IL15* expression (Fig. 5c). These observations suggest an important function for IL-15-regulated ILC1s in surveillance of breast cancers driven by *PIK3CA* gain-of-function mutations.

We wished to further decipher the cellular mechanisms by which IL-15 regulates tissue-resident innate lymphocytes in the tumor microenvironment, and used a transgenic mouse model of breast cancer driven by the murine polyomavirus middle tumor antigen (PyMT)[7] that activates PI3K[27], and thus models *PIK3CA* gain-of-function mutations. Our previous studies have revealed that tissue-resident cytotoxic ILC1-like innate lymphocytes expand in mammary tumors of PyMT mice[7]. To profile tumor-associated innate lymphocytes in an unbiased manner, we performed single-cell RNA sequencing experiments of $CD3^{-}NK1.1^{+}$ group 1 innate lymphocytes from PyMT tumors, and identified two major innate lymphocyte clusters, mouse NK (mNK) and mouse ILC1 (mILC1) (Fig. 5d and Supplementary Table 1). Gene set enrichment analysis (GSEA) revealed significant enrichment of differentially expressed DEGs between mNK and mILC1 clusters in the human NK and ILC1 DEG dataset (Fig. 5e), suggesting broad similarity between the murine and human clusters. Indeed, similar to their human counterparts, cluster mNK expressed higher levels of *S1pr5* and *Klf2*, while cluster mILC1 had higher expression of the tissue residency marker *Itga1* and *Zfp683* (Fig. 5f). Yet, expression of granzymes diverged through evolution with *Gzmc* and *Gzmb* transcripts enriched to different degrees in cluster mILC1 (Fig. 5g). We confirmed by flow cytometry that $CD49a^{+}CD103^{+}$ ILC1s had highest co-expression of granzyme C and granzyme B, while $CD49a^{-}CD103^{-}$ NK cells expressed only low levels of granzyme B (Fig. 5h). Compared to healthy mammary glands, transformed mammary tissues were enriched for ILC1s within the $CD3^{-}NK1.1^{+}$ innate lymphocyte compartment in association with increased expression of IL-15 (Fig. 5i–j). These findings suggest that $NK1.1^{+}CD49a^{+}CD103^{+}$ ILC1s represent the murine equivalent of human $CD56^{+}CD49a^{+}CD103^{+}$ ILC1s with their induction similarly associated with increased expression of IL-15 in tumor.

## ILC1s do not depend on DC or macrophage IL-15

To investigate which cell types expressed IL-15 in tumor, we employed an IL-15 enhanced green fluorescent protein (eGFP) reporter mouse strain with eGFP transcription and translation under the control of the *Il15* gene locus (IL-15$^{2A\text{-}eGFP}$)[28] (Extended Data Fig. 6a). To interrogate the exact cellular sources of IL-15 that promotes tissue-resident innate lymphocyte responses in tumor, we utilized a mouse strain harboring an exon 5-floxed allele of the *Il15* gene (*Il15*$^{fl}$) that could be inactivated by breeding with Cre recombinase transgenic mouse lines to target various immune cells, tumor stromal cell populations, and cancer cells (Extended Data Fig. 6b–d).

Using a conditional knockout *Il15ra* mouse strain, previous studies revealed that dendritic cells (DCs) and macrophages provide a critical source of IL-15 in support of homeostasis of circulating NK cells[29]. Two prominent macrophage populations, tumor-associated macrophages (TAMs) and mammary tissue macrophages (MTMs)[30], along with two conventional DC1 and DC2 subsets, were detected in PyMT tumors (Extended Data Fig. 6e). eGFP reporter analysis showed that MTMs and XCR1$^{+}$ DC1s expressed higher levels of IL-15, followed by TAMs and CD11b$^{+}$ DC2s in IL-15$^{2A\text{-}eGFP}$PyMT mice (Extended Data Fig. 6f). To investigate the function of IL-15 produced by these cells, we crossed *Il15*$^{fl/fl}$PyMT mice with *Itgax*-Cre transgenic mice that target DCs and TAMs (Extended Data Fig. 6g–h)[30]. Surprisingly, IL-15 loss in DCs and macrophages had no significant effect on the abundance of CD3$^{-}$NK1.1$^{+}$ cells or the CD49a$^{+}$CD103$^{+}$ ILC1 subset in tumors of *Itgax*-Cre*Il15*$^{fl/fl}$PyMT mice (Extended Data Fig. 6i–j). Furthermore, there was no difference in granzyme B and granzyme C expression in ILC1s (Extended Data Fig. 6k–l). In line with these findings, there was no difference in tumor burden in *Itgax*-Cre*Il15*$^{fl/fl}$PyMT mice compared to controls (Extended Data Fig. 6m). Consistent with previous studies[29], splenic NK cells, in particular the mature DX5$^{+}$CD27$^{-}$CD11b$^{+}$ NK cell subset, were reduced in *Itgax*-Cre*Il15*$^{fl/fl}$PyMT mice (Extended Data Fig. 6n–o). These findings demonstrate that IL-15 derived from CD11c$^{+}$ myeloid cell populations is dispensable for the induction of ILC1s in PyMT tumors.

## ILC1s do not depend on hematopoietic or stromal cell IL-15

We wished to expand IL-15 depletion with the *S100a4*-Cre line that targets various mesenchymal and hematopoietic cell lineages in adult tissues[31]. Using a *Rosa26*$^{LSL\text{-}YFP}$ Cre activity reporter line bred to the *S100a4*-CrePyMT background, we observed YFP expression in approximately 94% CD45$^{+}$ leukocytes, the majority of CD29$^{+}$EpCAM$^{-}$ stromal cells, and a subset of CD31$^{+}$ endothelial cells, but minimally in Ter119$^{+}$ erythrocytes or EpCAM$^{+}$ cancer cells in PyMT tumors (Extended Data Fig. 7a). eGFP reporter analysis of IL-15$^{2A\text{-}eGFP}$PyMT mice revealed that in addition to DCs and macrophages, Ly6G$^{+}$ neutrophils, NK1.1$^{+}$ innate lymphocytes, CD19$^{+}$ B cells, CD3$^{+}$ T cells, CD29$^{+}$EpCAM$^{-}$ stromal cells, and CD31$^{+}$ endothelial cells in PyMT tumors expressed varying amounts of IL-15 (Extended Data Fig. 7b).

To evaluate the function of IL-15 produced by *S100a4*-Cre-targeted cells, we bred *S100a4*-Cre mice to the *Il15*$^{fl/fl}$PyMT background which led to effective deletion of *Il15* in virtually all CD45$^{+}$ cells and CD29$^{+}$EpCAM$^{-}$ stromal cells (Extended Data Fig. 7c–d).

Unexpectedly, neither tumor CD3$^{-}$NK1.1$^{+}$ cells nor the CD49a$^{+}$CD103$^{+}$ ILC1 subset was substantially altered (Extended Data Fig. 7e–f). Granzyme B and granzyme C expression were also comparable in ILC1s, which was associated with comparable tumor burdens in *Il15*$^{fl/fl}$PyMT and *S100a4*-Cre*Il15*$^{fl/fl}$PyMT mice (Extended Data Fig. 7g–i). As expected, splenic NK cells and specifically the mature DX5$^{+}$CD27$^{-}$CD11b$^{+}$ subset were greatly diminished in *S100a4*-Cre*Il15*$^{fl/fl}$PyMT mice (Extended Data Fig. 7j–k). Together, these findings suggest that hematopoietic and stromal sources of IL-15 are of no consequence to the induction and function of ILC1s in PyMT tumors.

## ILC1s interact with and directly sense cancer cells

We wished to define the precise cellular niche in support of tissue-resident innate lymphocyte responses in tumor. Considering that granzyme C was selectively expressed in CD49a$^{+}$CD103$^{+}$ ILC1s (Fig. 5g–h), we generated an iCre recombinase reporter mouse line in which expression of iCre and a tandem dimer of Tomato (tdT) reporter was under the control of the *Gzmc* gene locus[32] (Extended Data Fig. 8a). We verified that tdT was expressed exclusively in the CD49a$^{+}$CD103$^{+}$ ILC1 subset of CD3$^{-}$NK1.1$^{+}$ innate lymphocytes and faithfully reported granzyme C protein expression (Extended Data Fig. 8b). To interrogate the distribution of granzyme C-expressing cells in reference to the epithelial cell lineage, we crossed *Gzmc*$^{tdT\text{-}T2A\text{-}iCre}$ mice to a E-Cadherin reporter mouse line that harbors a monomeric cyan fluorescent protein (mCFP) expression cassette under the control of the *Cdh1* gene locus (Extended Data Fig. 8c), which were further bred to the PyMT background. Mammary tissues were isolated from these mice and stained for the expression of PyMT oncoprotein to identify transformed mammary epithelial cells. Intriguingly, GzmC$^{tdT}$-expressing cells accumulated within PyMT-positive transformed areas of mammary tissues in close contact with E-Cadherin$^{mCFP}$-expressing cancer cells, and were rarely detected in PyMT-negative non-transformed epithelia (Fig. 6a). Notably, immunofluorescence staining also revealed that the vast majority of CD3$^{-}$CD103$^{+}$ ILC1s were in direct contact with E-Cadherin-expressing cancer cells in chRCC patients (Extended Data Fig. 5d). Thus, the evolutionarily conserved tumor-elicited tissue-resident ILC1 response is characterized by close interactions between cancer cells and innate lymphocytes.

To further define the cell behavior of tissue-resident innate lymphocytes, we bred *Gzmc*$^{tdT\text{-}T2A\text{-}iCre}$*Cdh1*$^{mCFP}$PyMT mice to a mouse strain harboring a genetically encoded calcium indicator, GCaMP5 made of a circularly permutated green fluorescent protein fused to the calcium-binding protein calmodulin and a M13 peptide, along with a tdT reporter located 3’ of the housekeeping *Polr2a* gene preceded by a floxed-STOP cassette (Extended Data Fig. 8d). Cre expression driven by the *Gzmc*$^{tdT\text{-}T2A\text{-}iCre}$ allele would result in GCaMP5 expression in granzyme C-expressing cells, and activation signals causing calcium flux would result in the cells to flash green (Extended Data Fig. 8e). To analyze these cells in real time, we performed live imaging experiments. GzmC$^{tdT}$-expressing cells appeared to be embedded within the tumor tissue in very close contact with E-Cadherin$^{mCFP}$-expressing cancer cells (Fig. 6b and Supplemental Video). Despite being stationary within the tumor tissue during the time window of imaging, the cells were active as demonstrated by frequent $Ca^{2+}$ flux events (Fig. 6b and Supplemental Video). These observations suggest that ILC1s directly sense cancer cells.

### Cancer cell-expressed IL-15 dictates ILC1 responses in tumor

As ILC1s appear to interact with and directly sense cancer cells, we explored the possibility that cancer cells themselves might be the source of IL-15 driving the cancer immunosurveillance response. To determine whether IL-15 was induced following cell transformation, we analyzed eGFP reporter expression in $CD24^{+}CD29^{+}EpCAM^{+}$ epithelial cells from mammary glands of $IL\text{-}15^{2A\text{-}eGFP}$ mice or mammary tumors of $IL\text{-}15^{2A\text{-}eGFP}$PyMT mice (Extended Data Fig. 9a). Of note, a higher level of eGFP reporter was detected in cancer cells compared to non-transformed mammary epithelia (Fig. 7a), implying that the enhanced IL-15 level in tumor tissue (Fig. 5j) was due to the increased IL-15 expression in cancer cells.

To target cancer cells, we utilized *S100a8*-Cre transgenic mice that marked more than 80% of transformed mammary epithelial cells as read out by crossing the *S100a8*-Cre line to a $Rosa26^{LSL\text{-}YFP}$ on the PyMT background (Extended Data Fig. 9b). To investigate the function of cancer cell-derived IL-15, we crossed *S100a8*-Cre mice to the $Il15^{fl/fl}$PyMT background, which led to effective deletion of *Il15* gene in cancer cells (Extended Data Fig. 9c). Strikingly, although splenic NK cells were unaffected in *S100a8*-Cre$Il15^{fl/fl}$PyMT mice (Extended Data Fig. 9d–e), total $CD3^{-}NK1.1^{+}$ innate lymphocytes and the $CD49a^{+}CD103^{+}$ ILC1 subset were severely reduced in tumors from these mice (Fig. 7b–c). In addition, the remaining tissue-resident innate lymphocytes had reduced expression of granzyme B and granzyme C (Fig. 7d–e), suggesting decreased cytotoxic activity. Accompanying these cellular defects, *S100a8*-Cre$Il15^{fl/fl}$PyMT mice displayed significant acceleration of tumor growth compared to controls (Fig. 7f). Collectively, these findings demonstrate that cancer cell-derived IL-15 regulates the expansion and effector function of tissue-resident cytotoxic ILC1s, and the lack of these effector cells results in impaired cancer immunosurveillance.

## DISCUSSION:

Cytotoxic immune cells are able to detect malignant cells and eliminate them in the process of cancer immunosurveillance. In this study, we found that while phenotypically exhausted $CD8^{+}$ T cells accumulated selectively in ccRCC tumors, tissue-resident ILC1s were induced in both ccRCC and chRCC tumors. The ILC1 response could effectively restrain chRCC, but not ccRCC, cancer progression with the level of IL-15 expressed in the tumor tissue being a key determinant. Cell culture experiments showed that a high concentration of IL-15 promoted the cytotoxic activities of ILC1s, and genetic studies using a murine tumor model demonstrated that cancer cell- but not stromal or hematopoietic cell-produced IL-15 supported the ILC1 response. Together, these findings reveal a conserved anti-tumor immune response in mice and humans mediated by cytotoxic tissue-resident innate lymphocytes in solid tumors with cancer cell-expressed IL-15 functioning as a rheostat to control the immunosurveillance outcome.

Single-cell RNA sequencing and cell-surface marker profiling experiments revealed two classes of tumor-induced lymphocyte responses in RCC. While ccRCC tumors had accumulation of exhausted $CD8^{+}$ T cells and expansion of ILC1s, both responses were associated with worse outcome across the ccRCC TCGA cohort. Chromophobe tumors on the other hand generally did not have a $CD8^{+}$ T cell response but instead had a striking

accumulation of ILC1s, a gene signature of which was associated with better overall survival in the chRCC TCGA dataset. Previous studies of group 1 innate lymphocytes in RCC have been limited to the ccRCC subtype with no clear ramification on patient outcome[33]. In addition, although $CD56^{bright}CD49a^{+}CD103^{+}$ innate lymphocytes have been found in human colorectal and lung tumors, their role in modulating cancer progression is unclear[34]. Thus, our findings are the first to reveal a tumor suppressor function of tissue-resident ILC1s in human cancer.

The differential prediction outcomes of the ILC1 signature on ccRCC and chRCC tumors as well as breast tumors with or without *PIK3CA* gain-of-function mutations imply tumor-subtype specific regulation. Of note, compared to ILC1s from adjacent normal kidney, granzyme A expression was specifically induced in ILC1s from chRCC, but not ccRCC, tumors. These findings imply that the cytotoxic potential of ILC1s is a critical determinant of their anti-tumor function, which is in agreement with our previous report of the cytolytic granule-mediated cancer immunosurveillance function of tissue-resident ILC1s in transgenic models of murine epithelial cancers[7]. Notably, in a carcinogen-induced murine fibrosarcoma model, ILC1s may promote cancer progression as a likely consequence of increased production of pro-angiogenic molecules[35]. Thus, heterogeneous or even opposing functional programs can be elicited by tissue-resident innate lymphocytes in tumors, which could be due to tumor types with epithelial cancers, but not mesenchymal fibrosarcoma, subject to ILC1-mediated cancer immunosurveillance. Nonetheless, it remains to be determined whether negative prognosis of the ILC1 signature on ccRCC patients reflects a pro-tumor function as suggested by a recent study[36]. Alternatively, the ILC1 response may be inconsequential, and the adverse association is simply because it tracks with disease progression.

An important regulator of the cancer immunosurveillance function of ILC1s was IL-15. IL-15 promoted expression of granzyme A and CD56, two markers enriched in ILC1s from chRCC tumors, as well as their cytotoxic activities against cancer cells. In the TCGA chRCC patient cohort, IL-15 expression was positively associated with the ILC1 signature, and stratified patients for survival probability. While both ccRCC and chRCC had increased abundance of ILC1s compared to normal kidney and blood, expression of IL-15 trended higher in chRCC tumors compared to ccRCC tumors. Prominent infiltration of phenotypically exhausted $CD8^{+}$ T cells that express high levels of the IL-15 receptor complex might also compete with ILC1s for IL-15 in ccRCC tumors, while ILC1s in chRCC tumors that concurrently lack $CD8^{+}$ T cells may not be subject to such competition. Together, these data imply that there is a mechanism of quantitative sensing for IL-15, in which low levels may allow for induction of ILC1s, as in the case of ccRCC, but high levels are required for the activation and acquisition of a cytotoxic effector program with potential functional impact on tumor control as observed for chRCC.

As the IL-15-dependent ILC1-mediated cancer immunosurveillance response is conserved between mice and men, we sought to define the cellular mechanisms of tumor IL-15 sensing in a murine model of breast cancer. We found that despite their abundant expression, hematopoietic and mesenchymal stromal cell sources of IL-15 were dispensable for the maintenance and activity of ILC1s. Instead, loss of IL-15 from epithelial cancer cells

resulted in loss of ILC1s in terms of abundance and their anti-tumor function. Such a cell type-specific function of IL-15 is likely due to the intraepithelial localization of ILC1s as well as IL-15 trans-presentation by IL15Rα on the surface of a source cell, thus triggering juxtacrine signaling[37, 38]. IL-15 expression is regulated at transcriptional and posttranscriptional levels[39]. Future studies will unravel how oncogenic pathways modulate its expression in cancer cells, which may help reveal the fundamental nature of such a cancer cell-extrinsic tumor suppressor pathway. Notably, loss of the *IL15* gene in colon cancer has been associated with reduced lymphocyte proliferation and poor patient outcome[40]. A recent study has also revealed that *IL15* loss occurs in colon cancer metastases that are not subject to adaptive lymphocyte-mediated immunoediting[41], raising the intriguing possibility that innate lymphocyte sensing of cancer cell-expressed IL-15 plays a critical tumor suppressor function not only in primary tumor growth but also in cancer cell dissemination.

Together, our study uncovers an innate lymphocyte-mediated epithelial cancer immunosurveillance mechanism whereby cancer cell-expressed IL-15 functions as an alarmin to be sensed by tissue-resident cytotoxic ILC1s. As innate lymphocytes and IL-15 are both actively explored in the clinic for cancer treatment, these findings suggest that distinct lineages or differentiation states of innate lymphocytes and the method of IL-15 delivery should be taken into consideration for effective cancer immunotherapy.

## METHODS:

### Human subjects and tissue collection

All research activities were preapproved by the Institutional Ethics Review Board at Memorial Sloan Kettering Cancer Center (protocol# 12–237) and individuals were required to provide written informed consent to participate in the study. All histological diagnoses were confirmed by expert genitourinary pathologists. Blood samples were collected in cellular preparation tubes (CPT) just prior to surgery. Tumor and adjacent normal kidney samples were directly obtained from the operating room during nephrectomy. Tissue samples were placed in separate labeled containers containing Roswell Park Memorial Institute (RPMI) medium and transported in regular ice to the laboratory. The CPTs were transported at 4°C. Overall transit time in all cases was less than 1 hour (from specimen extraction to cell dissociation) and the tissue samples were always kept in this medium. The cohort of ccRCC patients from which tissues were analyzed were 73.3% male, mean age 58.6, median age 58. The cohort of chRCC patients from which tissues were analyzed were 40% male, mean age 53.7, median age 58. For single-cell RNA sequencing, only tumor tissue was collected. The ccRCC patient was a 57-year-old female with stage IV disease and was treatment-naïve at the time of sample collection. The chRCC patient was an 84-year-old female with stage III disease and was treatment-naïve at the time of sample collection.

### Mice

All *in vivo* mouse experimental procedures were performed under the Sloan Kettering Institute (SKI) Institutional Animal Care and Utilization Committee (IACUC) - approved protocol 07-06-008. Mice were housed in specific pathogen-free animal facilities. Only female mice were used in this study. Littermates were used in all experiments, when

possible, otherwise age-matched cage mates were used. *Itgax*-Cre, *S100a4*-Cre, *S100a8*-Cre, *Rosa26*$^{LSL\text{-}YFP}$, *Cdh1*$^{mCFP}$ and GCaMP5 (also known as PC-G5-tdT) mice were obtained from Jackson Laboratories. *Gzmc*$^{tdT\text{-}T2A\text{-}iCre}$ mice were generated in the Li lab[32]. IL-15$^{2A\text{-}eGFP}$ mice were previously described[28]. *Il15*$^{fl}$ mice were generated in the Ikuta lab and will be reported elsewhere. Briefly, the *Il15*$^{fl}$ allele was established by flanking exon 5 with two loxP sequences by standard homologous recombination in embryonic stem cells (schematic provided in Extended Data Fig. 6c).

## Immune cell isolation from human and mouse tissues

Human blood was transferred from CPT tubes to 50 ml conical tubes containing red blood cell (Ammonium-Chloride-Potassium, ACK) lysis buffer and incubated for 10 minutes at 4°C. Tubes were spun at 860 g for 3 minutes, pellets were resuspended in FACS buffer (1x PBS with 1% FBS, 2mM EDTA and 0.02% sodium azide) and stored on ice until staining procedure. Human tumor and adjacent normal kidney tissues, as well as mouse mammary glands and tumors, were prepared by mechanical disruption via mincing with a razor blade followed by treatment with 280 U/ml Collagenase Type 3 (Worthington Biochemical) and 4 μg/ml DNase I (Sigma) in HBSS medium at 37°C for 1 hour with periodic short vortexing. Digested tissues were mashed through 70-μm filters and collected by centrifugation. Cell pellet was resuspended in 44% Percoll, layered on top of 66% Percoll (Sigma), and centrifuged at 1,900 g for 30 minutes without brake. Cells at the Percoll interface were collected, washed and resuspended in FACS buffer for downstream assays.

## Tumor measurement

Tumors in PyMT mice were measured weekly using a caliper, beginning when a single tumor diameter reached approximately 3–4 mm with data collection randomized and blind to mouse genotype. Tumor volume was calculated using the equation $[(L \times W^2) \times (\pi/6)]$ where "L"=length and "W"=width. Individual tumor volumes were added together to calculate total tumor burden per mouse. Mice were euthanized before tumor burden reached 3,000 $mm^3$.

## Preparation of single-cell RNA sequencing libraries

A suspension of 10,000 FACS sorted live cells in 1X PBS (calcium and magnesium free) containing 0.04% BSA (Sigma) were used as input to the 10X chromium controller system (10x Genomics Inc., product code 120223). Cells were barcoded using the 10x™ GemCode™ Technology to separately index each cell's transcriptome by partitioning them into Gel Bead-in-EMulsions (GEMs). GEMs were generated by combining barcoded Single Cell 5' Gel Beads, RT Master Mix with cells, and Partitioning Oil on a microfluidic chip. The GEM RT reaction was performed in thermocycler (53°C for 45 minutes, 85°C for 5 minutes, 4°C hold overnight). After RT incubation, the GEMs were broken, and the first strand of cDNA was recovered using DynaBeadsR MyOne™ Silane beads. 2 – 50 ng of amplified cDNA and the target enriched product respectively were used as input for library construction. Fragmentation, end repair and A tailing were performed to obtain final libraries containing the P5 and P7 priming sites used in IlluminaR sequencing. High sensitivity DNA chips and the Agilent 2100 bioanalyzer (Agilent Technologies) were used for 5' gene expression quality control and quantification. Quality control was performed

twice before sequencing. The 5' gene expression library was sequenced on NovaSeq 6000 S1 with sequencing depth of approximately 300–500 million reads per sample. For the mouse dataset, live, $CD45^+CD3^-NK1.1^+$ innate lymphocytes from the pooled tumors of one PyMT mouse were sorted into 1X PBS containing 0.04% BSA. Library preparation, quality control and single-cell RNA sequencing were performed by the Integrated Genomics Operations Core of Sloan Kettering Institute at MSKCC.

## Batch effect correction and single-cell count matrix processing

Pre-processing of single-cell RNA sequencing fastq files was conducted using Cell Ranger v3.0.2 (10x genomics). Single-cell RNA sequencing reads were aligned to the hg19 reference genome (ref-version 3.0.0). The count matrix used for downstream analysis was generated using the Cell Ranger count function with parameter –expect-cells=3000 (filter_matrix output). Cells with > 20% of transcripts derived from mitochondrial genes were considered apoptotic and were thus excluded, and all mitochondrial genes were removed from the final count matrix. Ribosomal genes and the noncoding RNAs NEAT1 and MALAT1 were excluded[42]. Genes with mean raw count < 3.0 were removed from the analysis, and cells with ambiguous phenotypes based on differentially expressed genes were excluded. This resulted in a final count matrix of 7402 cells and 14362 genes for downstream analysis. We used Seurat v2.3.4 to perform standard library size and log-normalization. The mean library size was 2240 transcripts per cell. Mouse single-cell RNA sequencing data ($CD3^-NK1.1^+$) was processed with the same pipeline; 873 cells and 10670 genes remained after QC.

To mitigate potential batch effects in the human data with two patients, we used the mutual nearest neighbors method[43]. Log-normalized counts for each of the samples were used as input to the fastMNN() function from the R scran package[44] in Bioconductor with default parameters. The resulting batch-corrected PCA matrix was then input into Seurat using the SetDimReduction() function. The top 10 principal components were used as input for Louvain clustering using the FindClusters() function in Seurat at resolution 0.5[45, 46]. tSNE was used for cluster visualization. We computed differentially expressed genes using the Wilcox test in the FindMarkers() function in Seurat, and genes with log fold change > 0 and FDR $P < 0.05$ were considered significantly differentially expressed. The definition of significantly differentially expressed genes was the same in the mouse dataset. Log-normalized counts were used for tSNE marker plots, violin plots and heatmaps.

## Derivation of cell type signatures from single-cell RNA sequencing data

To interrogate TCGA bulk RNA sequencing data using single-cell RNA sequencing clusters, we sought to derive robust gene signatures from our single-cell RNA sequencing data. We generated two signatures- one for the innate lymphocyte cluster ILC1, and one for phenotypically exhausted T cells (clusters CD8_2A and CD8_2B combined). We first performed a pairwise differential expression analysis for each of these clusters- i.e., for the ILC1 cluster, we compared cluster ILC1 to each other cluster, and took the set of genes upregulated (FDR $P < 0.05$, log fold change > 0.3) in the ILC1 cluster in all 9 comparisons. We repeated this analysis for the combined clusters CD8_2A and CD8_2B. To ensure that signatures were comprised only of genes associated with immune cells and to enable robust

application to TCGA dataset, we used the data from the Cancer Cell Line Encyclopedia to filter out genes expressed in any cancer cell line using a cutoff of 4 RPKM as previously described[47]. Signatures were then applied to the bulk RNA sequencing data from the TCGA KICH (n = 66 total; 65 with both RNA-seq and clinical data) and KIRC (N = 534 with both RNA-seq and clinical data) cohorts using single-sample Gene Set Enrichment Analysis (ssGSEA) method using the R package GSVA, and patients were considered to be in the high group for each signature if the ssGSEA score exceeded the top quartile within each cancer type. We repeated the ILC1 signature associations with survival in the TCGA breast cancer (BRCA) cohort using all patients (N = 1102) or in a subset of patients (N = 231) with hotspot activating mutations (p.H1047R, p.E545K, p.E542K) in *PIK3CA*[48]. Mutation data for the TCGA were obtained in the form of MutSigCV calls from the Broad Institute GDAC portal. The significance of the association of each signature with overall survival—computed using the Cox regression—was using a log-rank test. For the correlation of the ILC1 signature and IL-15 expression, the signature was applied to TCGA bulk RNA-seq data using ssGSEA, and the resulting score was plotted against the normalized expression of IL-15.

### GSEA analysis

For the GSEA analysis comparing mouse innate lymphocytes to their human counterparts, we first assembled a list of all DEGs between the human ILC1 and NK cell clusters. We then computed DEGs as described above for the two clusters in the mouse dataset. We treated the human DEGs as a gene set, and the log fold changes from the mouse DEG analysis as a ranked list for input into a GSEA “preranked” analysis.

### Validation of the ILC1 gene signature using bulk RNA sequencing data

Immune and non-immune cell populations were sorted from chRCC and ccRCC patient tumor samples. Library preparation, quality control and bulk RNA sequencing were performed by the Integrated Genomics Operations Core of Sloan Kettering Institute at MSKCC. We validated the ILC1 signature by applying it to bulk RNA sequencing data from the sorted populations using ssGSEA. We assessed discrimination performance by measuring the area under the receiver operating characteristic (ROC) and precision recall (PR) curves, when using the ILC1 signature to discriminate ILC1 populations (N = 12) vs all others (N = 57). The areas under the ROC and PR curves were calculated using the PRROC package in R.

### Flow cytometry

For flow cytometry experiments (human and mouse), cells were pre-incubated with 2.4G2 mAb to block Fc$\gamma$R binding and then stained with panels of cell surface marker antibodies for 20 minutes on ice. Cells were washed 2x with FACS buffer and stained with LIVE/DEAD kit (Invitrogen) or Zombie Live/Dead kit (BioLegend) to exclude dead cells. Intracellular staining was carried out using the FoxP3/Transcription factor Fix/Perm Kit (Tonbo). All samples were acquired with a LSRII flow cytometer (Becton Dickinson) and analyzed with FlowJo software version 9.6.2 or 10.6.1 (Tree Star).

### Antibodies and reagents for flow cytometry

Fluorochrome conjugated antibodies against human CD45 (clone H130), CD49a (SR84), CD16 (3G8), and CD14 (M5E2) were purchased from BD Biosciences. Antibodies against human CD3 (OKT3), PD-1 (EH12.2H7), Granzyme A (CB9), CD56 (HCD56), CD49a (TS2/T), and CD103 (Ber-ACT8) were purchased from Biolegend. Anti-human CD15 (MMA) was purchased from eBioscience, now Thermo Scientific, and anti-human NKG2A (REA110) was purchased from Miltenyi Biotec. Anti-human CD8α (RPA-T8) and biotinylated anti-human CD3 (UCHT1) were purchased from Tonbo Biosciences. Fluorochrome conjugated antibodies against mouse CD45 (clone 30-F11), CD49a (Ha31/8), CD103 (M290), Ly6G (1A8), F4/80 (T45–2342), CD11b (M1/70), MHC class II A-A/I-E (M5/114/15/2), and CD11c (N418) were purchased from BD Biosciences. Fluorochrome conjugated antibodies against mouse CD3ε (17A2), NK1.1 (PK136), CD19 (D1/CD19), XCR1 (ZET), CD49b (DX5), Ter119 (Ter-119), CD29 (HmB1–1), and EpCAM (G8.8) were purchased from BioLegend. Fluorochrome conjugated antibodies against mouse/human granzyme B (GB11) was purchased from Invitrogen. Fluorochrome conjugated antibodies against mouse CD27 (LG.7F9), CD31 (390), and CD24 (M1/69) were purchased from eBioscience.

### FACS cell sorting

Immune cells isolated from either human or mouse tissues were resuspended in MACS buffer (1x PBS with 1% FBS and 100 U/ml Penicillin G and 0.1 mg/ml Streptomycin) with appropriate cell surface marker antibodies and incubated for 20 minutes on ice. Cells were washed 2x in MACS buffer and stained with LIVE/DEAD kit (Invitrogen) or Zombie Live/Dead kit (BioLegend) to exclude dead cells. Cells were sorted using the BD FACS Aria Cell Sorter. Samples were collected in RPMI with 10% FBS and processed immediately after sorting.

### *In vitro* cell culture

Sorted cells were pelleted and resuspended in T cell medium (RPMI supplemented with 10% FBS, 1 mM sodium pyruvate, non-essential amino acids (Gibco), 10 mM HEPES (pH 7.3), 55 μM 2-Mercaptoethanol, 100 U/ml Penicillin G and 0.1 mg/ml Streptomycin) with the indicated amount of IL-15/IL-15Rα complex (provided by Dr. Naikong Cheung, MSKCC). Cells were cultured for 7 days in U-bottom plates in a 37°C humidified incubator.

### Single-cell killing assay

Sorted innate lymphocyte populations were cultured for 7 days to recover from stress associated with cell sorting in T cell medium (RPMI supplemented with 10% FBS, 1 mM sodium pyruvate, non-essential amino acids (Gibco), 10 mM HEPES (pH 7.3), 55 μM 2-Mercaptoethanol, 100 U/ml Penicillin G and 0.1 mg/ml Streptomycin). Cells were supplemented with either 10 ng/ml or 100 ng/ml human IL-15/IL-15Rα complex for the duration of culture. Polydimethylsiloxane grids containing 50×50×50 $\mu m^3$ wells were applied to the bottom of an 8-well chamber plate which was then heated at 60°C for 30 minutes, cooled and the appropriate medium was added to each chamber (T cell media supplemented with 10 ng/ml or 100 ng/ml human IL-15/IL-15Rα complex). 1 μg/ml

propidium iodide (PI) was added to the medium to enable real-time labeling of dead cells. K562 cells were labeled with Cell-trace Violet (CTV) dye to facilitate their identification. Once labeled, K562 cells and effector innate lymphocytes were combined at a 1:1.5 ratio, mixed well, and added to the appropriate chamber well, which was then briefly spun down to place the cells within the wells. In general, individual wells contained 1 to 3 K562 cells. The chambers were imaged using a 20x objective lens (ZEN microscope) at 10-minute intervals for 12 hours. Brightfield, CTV and PI images were collected at each time point. Quantification was restricted to wells containing one effector cell in presence of at least one K562 cell in the same well. Only a single killing event per well was scored.

### IL-15 ELISA

Mammary tissues were collected from 8-week-old wild-type and PyMT mice, pooled, weighed and immediately snap frozen in liquid nitrogen and stored at −80°C. Frozen tissues were thawed on ice, placed in a glass petri dish on ice, and minced using two scalpels. Tissue pieces were transferred to Eppendorf tubes. 1X lysis buffer [10 mM Tris–HCl (pH 8.0), 150 mM NaCl, 1% NP-40, 10% Glycerol, 5. 5 mM EDTA, Protease inhibitor cocktail (Roche)] was added with the following formula: 5x weight tissue in mg = volume of lysis buffer in µl. Samples were homogenized using an Eppendorf-fitting pestle and lysates were incubated for 1 hour at 4°C while rotating. Lysates were then sonicated 7-minute regimen with 30-second intermittent on and off sonification periods at 4°C using the Diagenode Bioruptor. Samples were centrifuged at 700 g for 15 minutes. Supernatants were collected, protein concentration was determined, and samples were stored at −80°C. Protein lysate was diluted 1:50 and tested for IL-15 using a Mouse IL-15 ELISA Kit according to the manufacturer's recommendations (Sigma). Values obtained were multiplied by the dilution factor, IL-15 quantity in ng was calculated for 1 mg of tissue.

### IL-15 RT-PCR

Cells were directly sorted into TRIzol (Life Technologies). Total RNA was extracted with Direct-zol RNA MicroPrep kit (Zymo Research), and then reverse-transcribed to cDNA with Maxima First Strand cDNA synthesis Kit (Thermo Scientific). Quantitative PCR was performed with mouse *Il15*-specific primers (forward, 5'-ACATCCATCTCGTGCTACTTGT-3'; reverse, 5'-GCCTCTGTTTTAGGGAGACCT-3'). *Il15* expression data were normalized relative to *Gapdh* expression, and relative quantification levels were calculated.

### Intravital confocal microscopy

At 12 weeks of age, intravital confocal microscopy of mammary tumors was performed. Briefly, mice were anaesthetized using a cocktail of ketamine and xylazine. Anaesthesia was maintained by continuous inhalation of 0.5% isoflurane and mice were kept to 37°C and received oxygen (0.5 L/minute). The fur from the lower flank region was trimmed and the area sterilized using Betadine solution. The fourth left or right mammary gland was surgically exposed with a ventral skin incision and a skin flap. The mouse was transferred to a stage heated to 37°C. All imaging was done on an Olympus FVMPE-RS upright Multiphoton microscope fitted with a 25×1.05NA Plan water-immersion objective and a Mai-Tai DeepSee Ti-Sapphire laser (Spectraphysics). Imaging was performed using λ = 910

nm excitation and fluorescence emission was collected in three channels, using the following filter sets: a filter (480/40 nm) for CFP, a second filter (540/20 nm) for GFP and a third filter (605/70 nm) for tdTomato detection. Time-lapse images were acquired by scanning at 1,024 × 1,024 pixels with a z-step size of 3–4 μm and a total z-volume 50–100 μm, at 30 to 60 seconds intervals.

### Immunofluorescence of formalin-fixed paraffin-embedded (FFPE) tissue

Tumor tissues were paraffin embedded and sliced by the Molecular Cytology Core Facility at MSKCC. Tumor slices were de-paraffinized and rehydrated as following: three 5-minute washes in HistoClear, two 10-minute washes in each of the following ethanol concentrations – 100%, 90%, 70%, and 50% followed by two 5-minute washes in distilled water. Antigen retrieval was performed by bringing slides to a boil in 10 mM sodium citrate buffer (pH 6.0) and maintained at sub-boiling temperature for 10 minutes in the microwave, then cooled at 4°C for 30 minutes. Slides were washed twice for 5 minutes in distilled water. Endogenous peroxidase activity was quenched with 3% hydrogen peroxide in methanol for 30 minutes at 4°C then washed twice for 5 minutes in distilled water. Tissues were permeabilized by washing twice for 10 minutes in 1% animal serum in PBS with 0.4% Triton X-100 (PBS-T) followed by blocking for non-specific binding by incubating the tissue sections with 5% animal serum in PBS-T for 30 minutes at 4°C. Primary antibodies against CD103 (clone EPR4166, Abcam catalog number ab29202, concentration 1:100) and E-Cadherin-AF647 (clone EP700Y, Abcam catalog number ab194982, concentration 1:100) were added in PBS-T and incubated overnight at 4°C in a humidified chamber. Slides were washed twice in PBS-T and stained with secondary antibody (goat anti-rabbit AF488, Life Technologies catalog number A11034, 1:1000) for 1 hour at 4°C. Slides were washed twice in PBS-T and stained with DAPI then mounted with OmniMount (National Diagnostics catalog number HS-110). Slides were imaged with an upright widefield microscope with a 40X objective and images collected with Pannoramic Scanner Software 2.0. Images were pseudocolored and processed with FIJI software.

### Immunofluorescence of frozen tissue

Tumors were harvested from E-Cadherin$^{CFP}$GzmC-iCre$^{tdT}$PyMT mice and fixed in Periodate-Lysine-Paraformaldehyde (PLP) for 16–24 hours, 30% sucrose for 24 hours, then frozen in OCT. Tissue was sectioned at 20 μm thickness, blocked for 30 minutes and stained with Hoechst and a fluorescently conjugated antibody against PyMT (Thermo Fisher Scientific, catalog number MA1–46061) overnight at 4°C. Slides were washed and stained with secondary antibody (goat anti-rat AF488, Life Technologies catalog number A-11006). Images were taken on confocal microscope using 4 color channels.

### Statistical analysis

Spearman's correlation, log-rank and Wilcoxon tests were used to calculate statistical significance where appropriate. Two tailed unpaired t tests, ratio paired t tests, and one-way ANOVA were conducted using Prism 8 software. A value of $P < 0.05$ was considered statistically significant. No statistical methods were used to pre-determine sample sizes but our sample sizes are similar to those reported in a previous publication[7]. Data distribution was assumed to be normal but was not formally tested.

## Extended Data

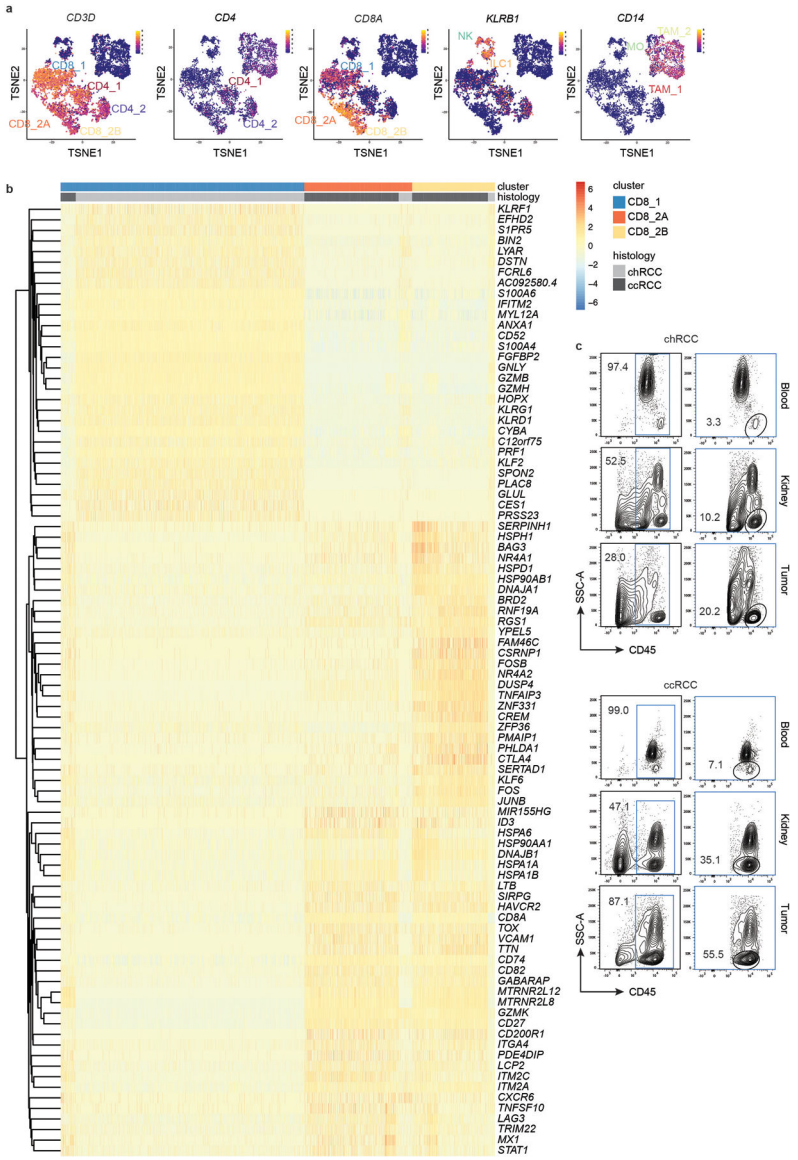


**Extended Data Fig. 1. Cluster-defining marker plots for all clusters and heatmap of differential gene expression analysis among the three CD8$^+$ T cell clusters**

**a,** Marker plots showing normalized expression of selected common markers for lymphoid and myeloid populations (*CD3D* – T cells, *CD4* – CD4$^+$ T cells, *CD8A* – CD8$^+$ T cells, *KLRB1* – innate lymphocytes, *CD14* – myeloid cells). **b,** Heatmap of expression of the top 30 differentially expressed genes by log fold change, [computed using Wilcox test in the FindMarkers() function of Seurat (FDR P <0.05 and LFC > 0)], across the three CD8$^+$ T cell clusters within the chromophobe renal cell carcinoma (chRCC) and clear cell RCC (ccRCC) patients. Each column represents an individual cell. **c,** Plots showing the back gating strategy for plots shown in Fig. 1e.

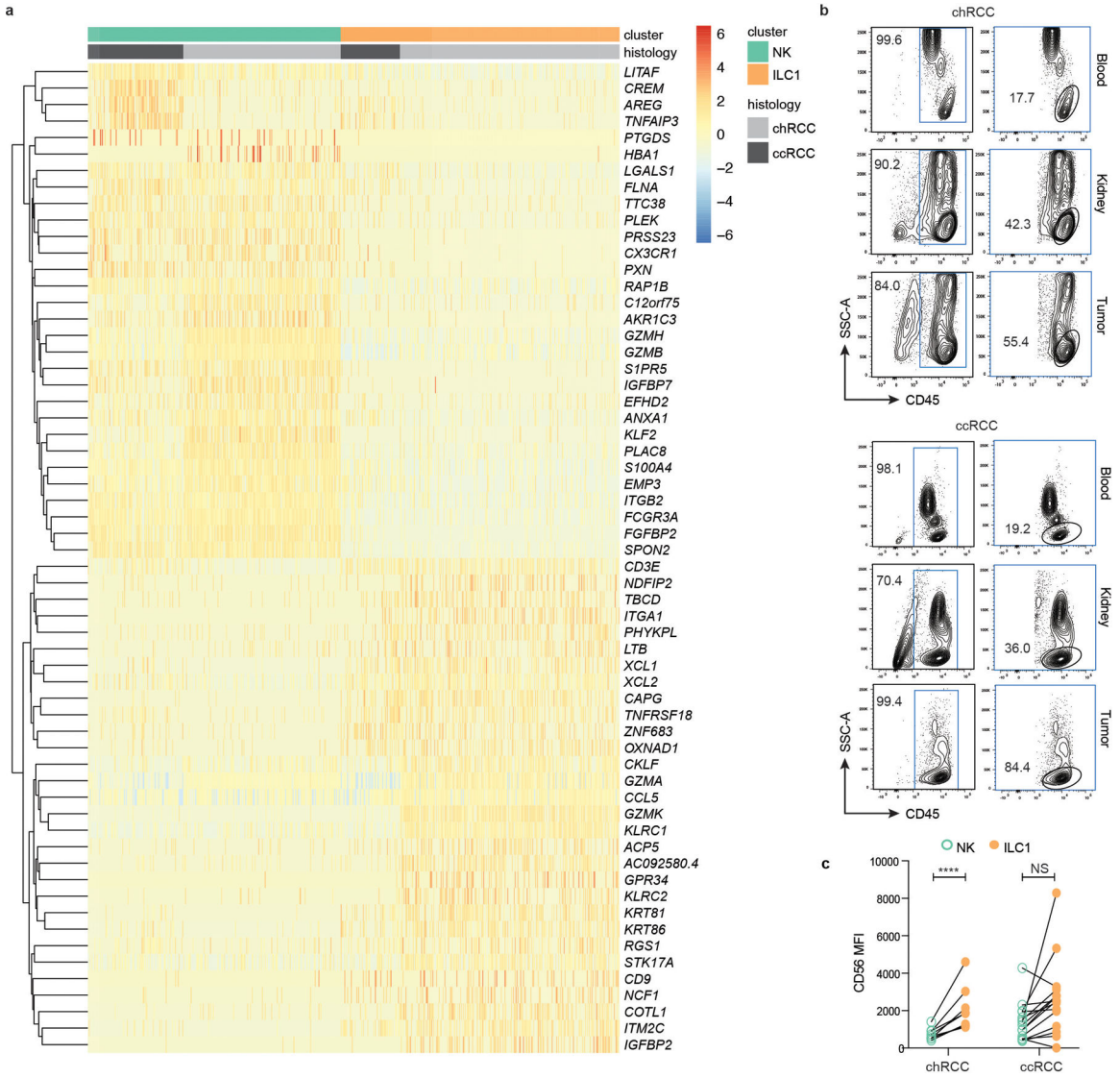


**Extended Data Fig. 2. Heatmap of differential gene expression analysis between clusters NK and ILC1 and comparison of CD56 expression between CD49a$^{+}$CD103$^{+}$ ILC1s and CD49a$^{-}$CD103$^{-}$ NK cells**

**a,** Heatmap of expression of the top 30 differentially expressed genes by log fold change, [computed using Wilcox test in the FindMarkers() function of Seurat (FDR P <0.05 and LFC > 0)], across the two innate lymphocyte clusters in the chromophobe renal cell carcinoma (chRCC) and clear cell RCC (ccRCC) patients. Each column represents an individual cell. **b,** Plots showing the back gating strategy for plots shown in Fig. 2c. **c,** CD56 MFI in CD49a$^{+}$CD103$^{+}$ ILC1s (orange) compared to CD49a$^{-}$CD103$^{-}$ NK cells (green) in the indicated histology. Each pair of symbols connected by a line denotes an individual patient (chRCC n = 9, ccRCC n = 15). Paired ratio t test was used for statistical analysis, NS = non-significant, ****p < 0.0001.

a

| Population | Defined as |
|---|---|
| CD16$^-$ Tissue Resident ILC1 | CD45$^+$CD3$^-$CD19$^-$CD56$^+$CD16$^-$CD49a$^+$CD103$^+$ |
| CD16$^+$ Tissue Resident ILC1 | CD45$^+$CD3$^-$CD19$^-$CD56$^+$CD16$^+$CD49a$^+$CD103$^+$ |
| CD16$^-$ Circulating NK cells | CD45$^+$CD3$^-$CD19$^-$CD56$^+$CD16$^-$CD49a$^-$CD103$^-$ |
| CD16$^+$ Circulating NK cells | CD45$^+$CD3$^-$CD19$^-$CD56$^+$CD16$^+$CD49a$^+$CD103$^+$ |
| Tissue Resident CD8 T cells | CD45$^+$CD3$^+$CD4$^-$CD8$^+$CD49a$^+$CD103$^+$ |
| Circulaing CD8 T cells | CD45$^+$CD3$^+$CD4$^-$CD8$^+$CD49a$^-$CD103$^-$ |
| CD4 T cells | CD45$^+$CD3$^+$CD4$^+$CD8$^-$ |
| Neutrophils | CD45$^+$CD3$^-$CD19$^-$CD16$^{high}$HLA-DR$^-$ |
| Regulatory T cells | CD45$^+$CD3$^+$CD4$^+$CD8$^-$CD25$^+$ |
| Non CD45$^+$ cells | CD45$^-$ |
| B cells | CD45$^+$CD3$^-$CD19$^+$ |
| CD1c$^+$ Dendritic Cells | CD45$^+$CD3$^-$CD19$^-$HLA-DR$^+$CD14$^-$CD16$^-$CD1c$^+$CD141$^-$ |
| CD141$^+$ Dendritic Cells | CD45$^+$CD3$^-$CD19$^-$HLA-DR$^+$CD14$^-$CD16$^-$CD1c$^-$CD141$^+$ |
| Macrophages | CD45$^+$CD3$^-$CD19$^-$HLA-DR$^+$CD14$^+$CD16$^+$ |
| Monocytes | CD45$^+$CD3$^-$CD19$^-$CD14$^+$ |

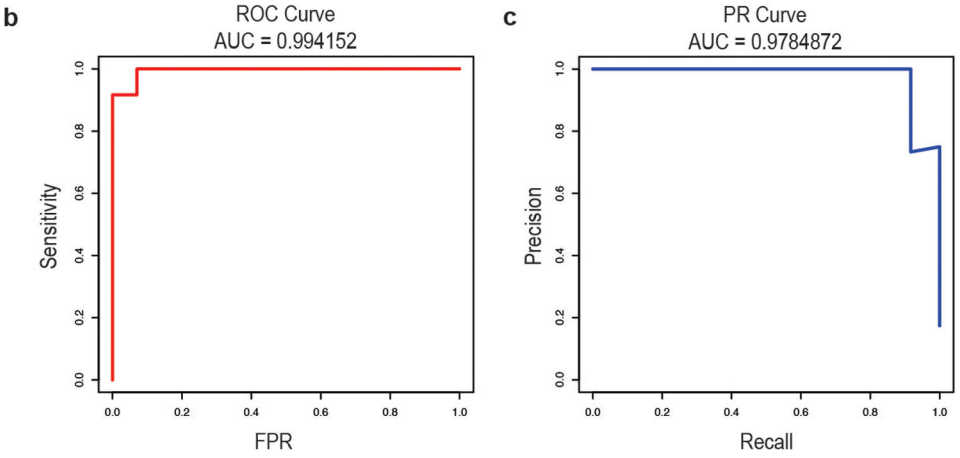


**Extended Data Fig. 3. Validation of the ILC1 signature**

**a,** Table outlining the cell surface markers used to define each immune cell population sorted for downstream bulk RNA-sequencing. **b,** Area under the ROC curve and **c,** precision recall curve, when using the ILC1 signature to discriminate resident ILC1 populations (n = 12) vs all others (n = 57). The areas under the ROC and PR curves were calculated using the PRROC package in R.

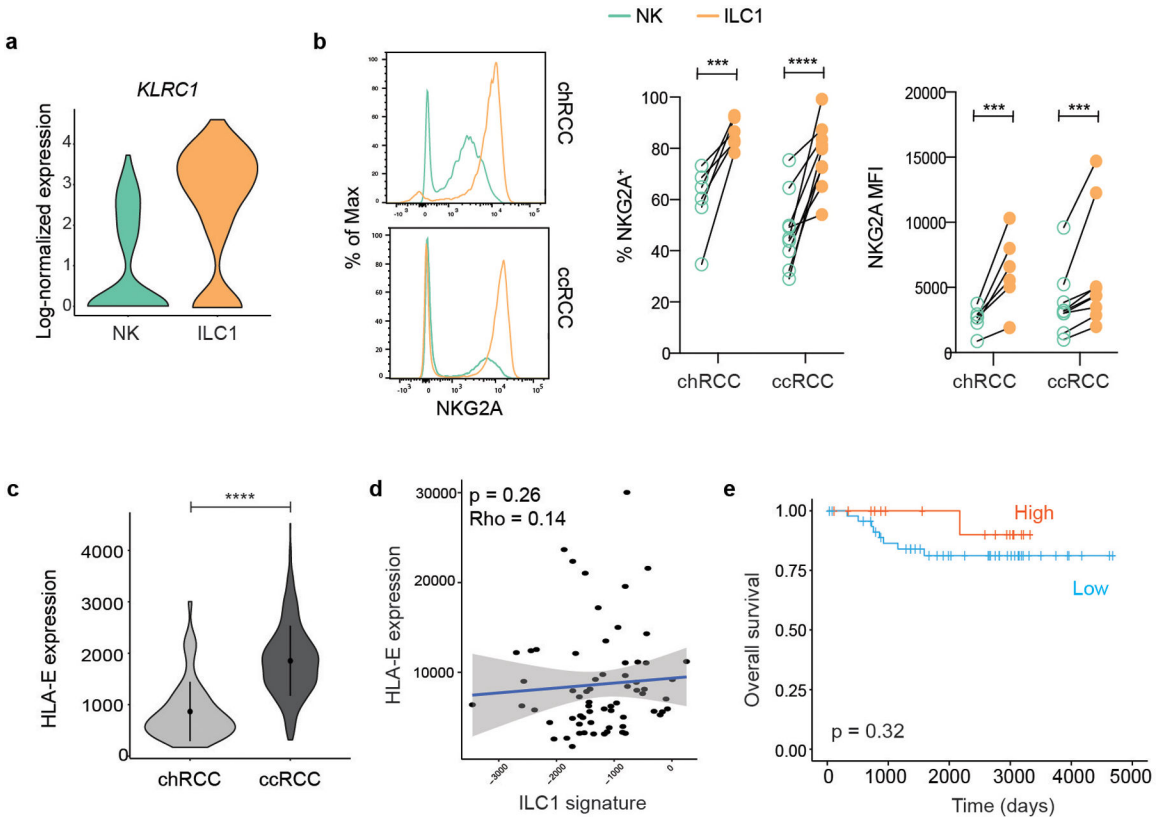


**Extended Data Fig. 4. CD49a$^{+}$CD103$^{+}$ ILC1s and CD49a$^{-}$CD103$^{-}$ NK cells are phenotypically distinct in terms of NKG2A and CD16 expression**

**a,** Violin plot showing *KLRC1* expression in the indicated clusters. **b,** (Left) Representative histograms of NKG2A expression in CD49a$^{-}$CD103$^{-}$ NK cells (green) and CD49a$^{+}$CD103$^{+}$ ILC1s (orange) from the same patient of the indicated histology. (Center) Quantification of NKG2A$^{+}$ cells within the indicated cell type and histology. (Right) MFI of NKG2A in NKG2A$^{+}$CD49a$^{+}$CD103$^{+}$ ILC1s compared to NKG2A$^{+}$CD49a$^{-}$CD103$^{-}$ NK cells in tumor samples. chRCC n = 6, ccRCC n = 9. Each pair of symbols connected by a line denotes an individual patient. Two-tailed unpaired t test was used for statistical analysis of the percent NKG2A positive, and paired ratio t test was used for statistical analysis of MFI, ***p < 0.001, ****p < 0.0001. **c,** Violin plot showing log-normalized expression of the *HLA-E* gene in the TCGA ccRCC and chRCC cohorts. Two-sided Wilcoxon test was used for statistical analysis $p < 2.2e^{-16}$. **d,** Correlation between level of HLA-E expression and ILC1 signature in chRCC cases from the TCGA database. Statistical analyses calculated using Spearman's correlation. Error bands represent the 95% confidence interval. **e,** Association of HLA-E expression and overall survival across the TCGA chRCC cohort. High represents the top quartile and low represents the bottom 3 quartiles of IL-15 expression level. P value calculated using a Cox regression and log-rank test.

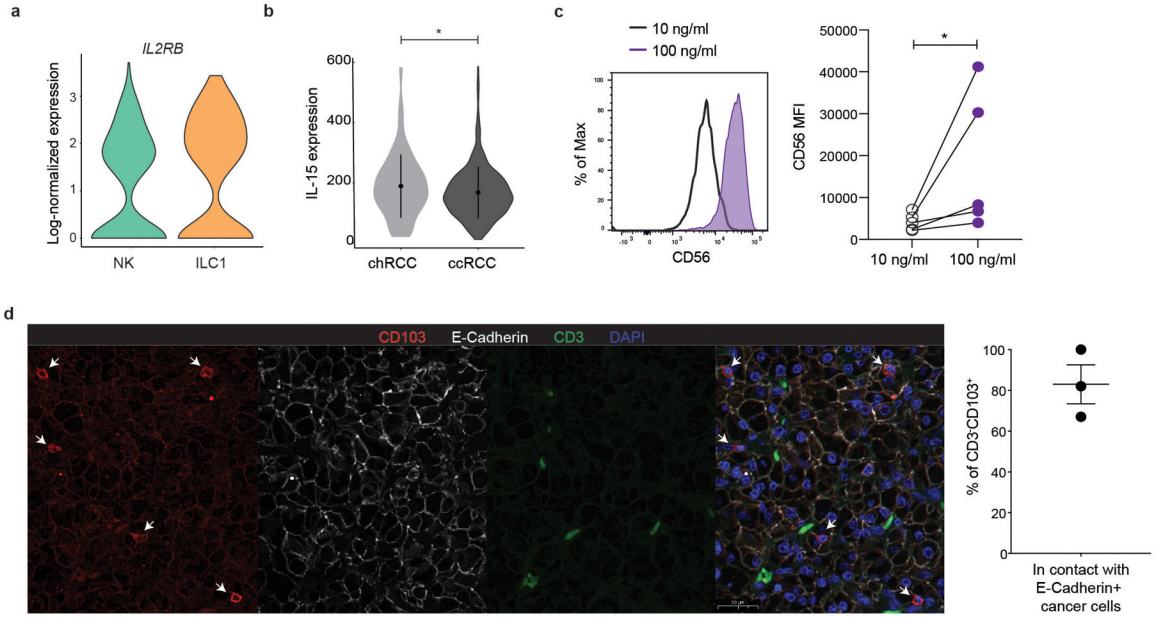


**Extended Data Fig. 5. *IL2RB* expression in clusters NK and ILC1, *IL15* expression in chRCC and ccRCC tumors from the TCGA, and IL-15 regulation of CD56 expression in CD49a$^{+}$CD103$^{+}$ ILC1s**

**a,** Violin plot showing log-normalized expression of the *IL2RB* gene in the indicated innate lymphocyte clusters. **b,** Violin plot showing level of *IL15* expression across chromophobe renal cell carcinoma (chRCC) and clear cell RCC (ccRCC) patients in the TCGA cohort. One-sided Wilcoxon test was used for statistical analysis, *p < 0.05. **c,** (Left) Representative histograms of CD56 expression in CD49a$^{+}$CD103$^{+}$ ILC1s treated with the indicated concentration of IL-15/IL-15Rα complex. (Right) MFI of CD56 in CD49a$^{+}$CD103$^{+}$ innate lymphocytes isolated from tumors treated with 100 ng/mL IL-15/IL-15Rα complex compared to 10 ng/mL IL-15/IL-15Rα complex. Each pair of symbols connected by a line denotes cells isolated from an individual patient (n = 5, 1 chRCC and 4 ccRCC), in 5 independent experiments. Paired ratio t test was used for statistical analysis, *p < 0.05. **d,** Representative images of chRCC tumor tissue that was stained with anti-CD103 (red), anti-E-Cadherin (white), anti-CD3 (green), and DAPI (blue). White arrows denote CD3$^{-}$CD103$^{+}$ innate lymphocytes. Scale bar = 20 μM. Quantification is representative of three independent chRCC patient tumor tissues, each dot represents one patient. Error bar represents mean ± SEM.

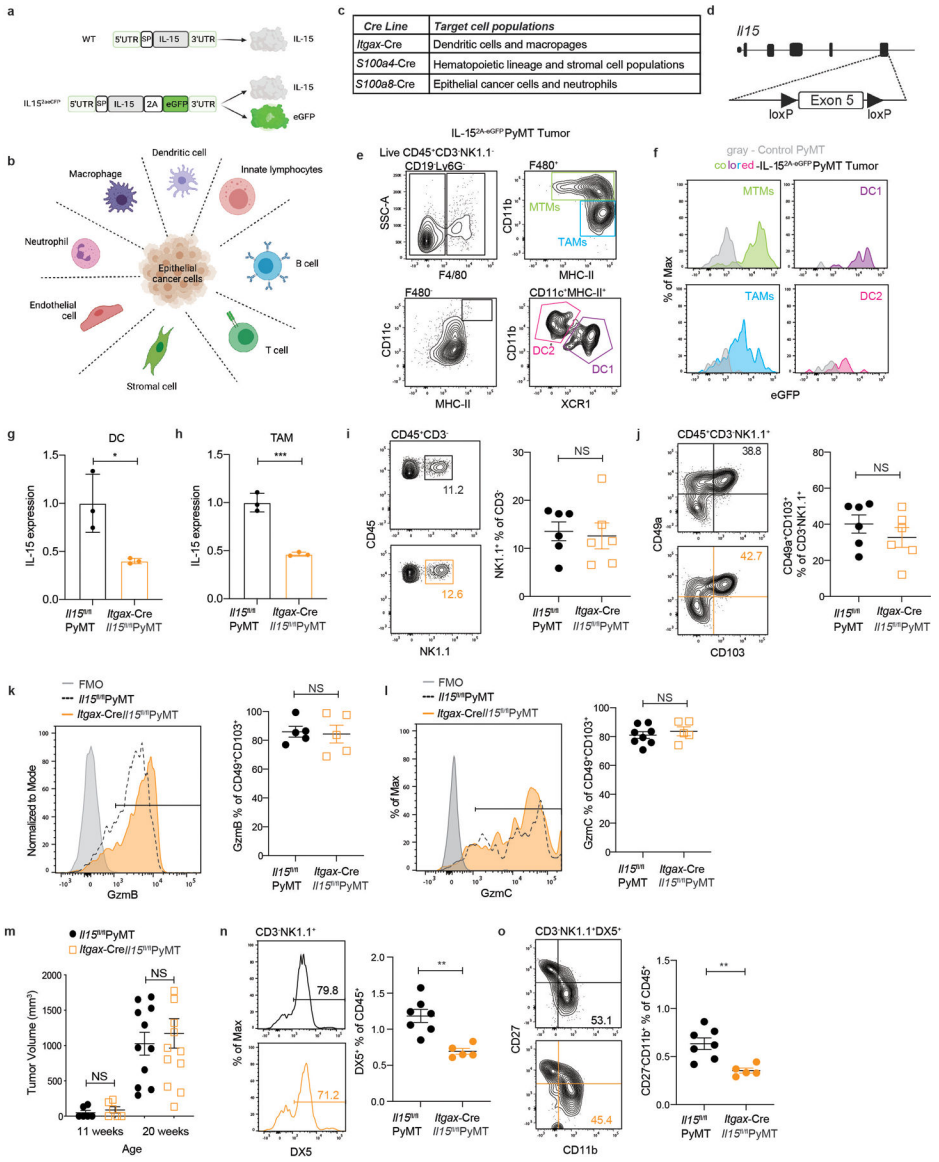


**Extended Data Fig. 6. ILC1s function independently of DC- and macrophage-expressed IL-15**

**a,** Schematic describing the IL-15$^{2A\text{-}eGFP}$ reporter mouse strain. **b,** Types of cancer cells and stromal cells with the potential for IL-15 expression in PyMT tumors. **c,** Table listing the Cre recombinase lines used to delete IL-15 in the listed target cell populations. **d,** Schematic of an *Il15* floxed allele. **e,** Gating strategy for determining eGFP expression in the indicated myeloid cell populations isolated from pooled tumors of a 20-week-old IL-15$^{2A\text{-}eGFP}$PyMT mouse. **f,** Flow cytometric analysis of eGFP expression in the indicated myeloid cell populations from pooled tumors of a 20-week-old IL-15$^{2A\text{-}eGFP}$PyMT (colored) or PyMT mouse (gray). **g,** qPCR analysis of *Il15* mRNA expression in sorted DCs from pooled tumors of 20–24-week-old *Il15*$^{fl/fl}$PyMT (n = 3) or *Itgax*-Cre*Il15*$^{fl/fl}$PyMT (n = 3) mice**. h,** qPCR analysis of *Il15* mRNA expression in sorted TAMs from pooled tumors of 20–24-week-old *Il15*$^{fl/fl}$PyMT (n = 3) or *Itgax*-Cre*Il15*$^{fl/fl}$PyMT (n = 3) mice**. i,** Representative plot and quantification of NK1.1$^{+}$ cells out of total CD45$^{+}$CD3$^{-}$ cells isolated from

pooled tumors of 20–24-week-old *Il15*$^{fl/fl}$PyMT (n = 6) or *Itgax*-Cre*Il15*$^{fl/fl}$PyMT mice (n = 6). **j,** Representative plot and quantification of percentage of CD49a$^{+}$CD103$^{+}$ ILC1s out of total CD45$^{+}$CD3$^{-}$NK1.1$^{+}$ cells isolated from pooled tumors of 20–24-week-old *Il15*$^{fl/fl}$PyMT (n = 6) or *Itgax*-Cre*Il15*$^{fl/fl}$PyMT (n = 6) mice. **k,** Representative histogram and quantification of granzyme B (GzmB) expression in CD49a$^{+}$CD103$^{+}$ ILC1s from pooled tumors of 20–24-week-old *Il15*$^{fl/fl}$PyMT (n = 5) or *Itgax*-Cre*Il15*$^{fl/fl}$PyMT (n = 5) mice. **l,** (Left) Representative histogram and quantification of granzyme C (GzmC) expression in CD49a$^{+}$CD103$^{+}$ ILC1s from pooled tumors of 20–24-week-old *Il15*$^{fl/fl}$PyMT (n = 8) or *Itgax*-Cre*Il15*$^{fl/fl}$PyMT (n = 5) mice. **m,** Total tumor burden of *Il15*$^{fl/fl}$PyMT (11 weeks n = 6, 20 weeks n = 11) and *Itgax*-Cre*Il15*$^{fl/fl}$PyMT (11 weeks n = 6, 20 weeks n = 11) mice monitored between 11 and 20 weeks of age. **n,** Representative histograms of CD49b (DX5) expression among total CD3$^{-}$NK1.1$^{+}$ cells in spleens of the indicated mouse genotype. (Right) Percentage of DX5$^{+}$ NK cells quantified out of total splenic CD45$^{+}$ immune cells (*Il15*$^{fl/fl}$PyMT n = 7, *Itgax*-Cre*Il15*$^{fl/fl}$PyMT n = 5). **o,** (Left) Representative plots of CD27 and CD11b expression among total CD3$^{-}$NK1.1$^{+}$DX5$^{+}$ NK cells in spleens of the indicated mouse genotype. (Right) Percentage of DX5$^{+}$CD11b$^{+}$CD27$^{-}$ cells quantified out of total splenic CD45$^{+}$ cells (*Il15*$^{fl/fl}$PyMT n = 7, *Itgax*-Cre*Il15*$^{fl/fl}$PyMT n = 5). **g-o,** Each dot represents an individual mouse. Data are pooled from 3 or more independent experiments. All error bars represent the mean ± SEM. Two-tailed unpaired t test was used for statistical analysis, NS = non-significant, *p < 0.05, **p < 0.01, ***p < 0.001.

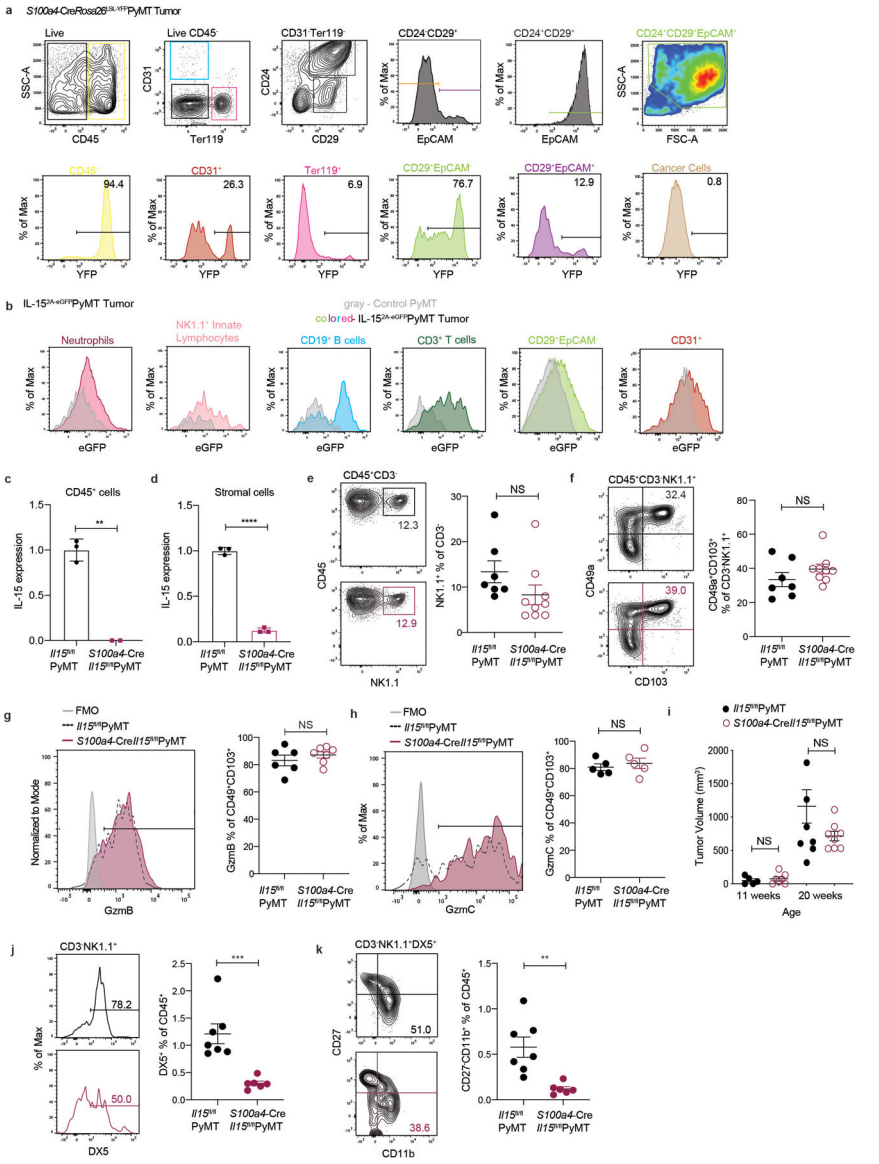

**Extended Data Fig. 7. ILC1s function independently of hematopoietic and stromal cell sources of IL-15**

**a,** Gating strategy and YFP expression in the indicated populations from pooled tumors of a 20-week-old *S100a4*-Cre*Rosa26*$^{LSL\text{-}YFP}$PyMT mouse. **b,** Flow cytometric analysis of eGFP expression in the indicated populations from pooled tumors of 20-week-old IL-15$^{2A\text{-}eGFP}$PyMT (colored) or control PyMT (gray) mice. **c,** qPCR analysis of *Il15* mRNA expression in sorted live CD45$^+$ immune cells from 20–24-week-old *Il15*$^{fl/fl}$PyMT (n = 3) or *S100a4*-Cre*Il15*$^{fl/fl}$PyMT (n = 2) mice. **d,** qPCR analysis of *Il15* mRNA expression in sorted live CD45$^-$CD31$^-$Ter119$^-$CD24$^-$CD29$^+$EpCAM$^-$ stromal cells from 20–24-week-old *Il15*$^{fl/fl}$PyMT (n = 3) or *S100a4*-Cre*Il15*$^{fl/fl}$PyMT mice (n = 3). **e,** Representative plot and quantification of percentage of NK1.1$^+$ cells out of total CD3$^-$ cells isolated from pooled tumors of 20–24-week-old *Il15*$^{fl/fl}$PyMT (n = 7) or *S100a4*-Cre*Il15*$^{fl/fl}$PyMT mice (n = 9). **f,** Representative plot and quantification of percentage of CD49a$^+$CD103$^+$ ILC1s out of total CD45$^+$CD3$^-$NK1.1$^+$ cells isolated from pooled tumors of 20–24-week-old

*Il15*$^{fl/fl}$PyMT (n = 7) or *S100a4*-Cre*Il15*$^{fl/fl}$PyMT (n = 9) mice. **g,** Representative histogram and quantification of granzyme B (GzmB) expression in CD49a$^{+}$CD103$^{+}$ ILC1s isolated from pooled tumors of 20–24-week-old *Il15*$^{fl/fl}$PyMT (n = 6) or *S100a4*-Cre*Il15*$^{fl/fl}$PyMT (n = 7) mice. **h,** Representative histogram and quantification of granzyme C (GzmC) expression in CD49a$^{+}$CD103$^{+}$ ILC1s isolated from pooled tumors of 20–24-week-old *Il15*$^{fl/fl}$PyMT (n = 5) or *S100a4*-Cre*Il15*$^{fl/fl}$PyMT (n = 5) mice. **i,** Total tumor burden of *Il15*$^{fl/fl}$PyMT (11 weeks n = 5, 20 weeks n = 7) and *S100a4*-Cre*Il15*$^{fl/fl}$PyMT (11 weeks n = 7, 20 weeks n = 8) mice monitored between 11 and 20 weeks of age. **j,** Representative histograms of CD49b (DX5) expression among total CD3$^{-}$NK1.1$^{+}$ cells in spleens of the indicated mouse genotype. (Right) Percentage of DX5$^{+}$ NK cells quantified out of total splenic CD45$^{+}$ cells (*Il15*$^{fl/fl}$PyMT n = 7, *S100a4*-Cre*Il15*$^{fl/fl}$PyMT n = 6). **k,** (Left) Representative plots of CD27 and CD11b expression among total CD3$^{-}$NK1.1$^{+}$DX5$^{+}$ NK cells in spleens of the indicated mouse genotype. (Right) Percentage of DX5$^{+}$CD11b$^{+}$CD27$^{-}$ cells quantified out of total splenic CD45$^{+}$ cells (*Il15*$^{fl/fl}$PyMT n = 7, *S100a4*-Cre*Il15*$^{fl/fl}$PyMT n = 6). **c-k,** Each dot represents an individual mouse. Data are pooled from 3 or more independent experiments. All error bars represent the mean ± SEM. Two-tailed unpaired t test was used for statistical analysis, NS = non-significant, **p < 0.01, ***p < 0.001, ****p < 0.0001.

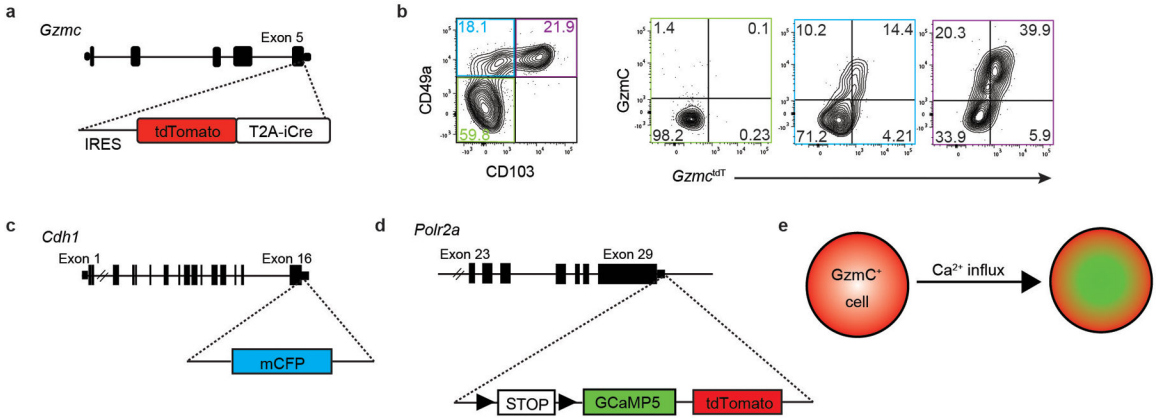


**Extended Data Fig. 8. Mouse models utilized for characterization of tissue-resident ILC1 responses in PyMT tumors**

**a,** Diagram denoting the *Gzmc* gene locus of *Gzmc*$^{tdT\text{-}T2A\text{-}iCre}$ mice. **b,** Flow cytometric analysis of GzmC$^{tdT}$ reporter expression and granzyme C protein expression among the indicated CD3$^{-}$NK1.1$^{+}$ innate lymphocyte populations in PyMT tumors. **c,** Diagram denoting the *Cdh1* gene locus of *Cdh1*$^{mCFP}$ mice. **d,** Diagram denoting the *Polr2a* gene locus harboring an expression cassette for a GCaMP5 calcium indicator and a tdT reporter. **e,** Expected fluorescent phenotype that results when calcium signaling is sensed in GCaMP5-expressing innate lymphocytes.

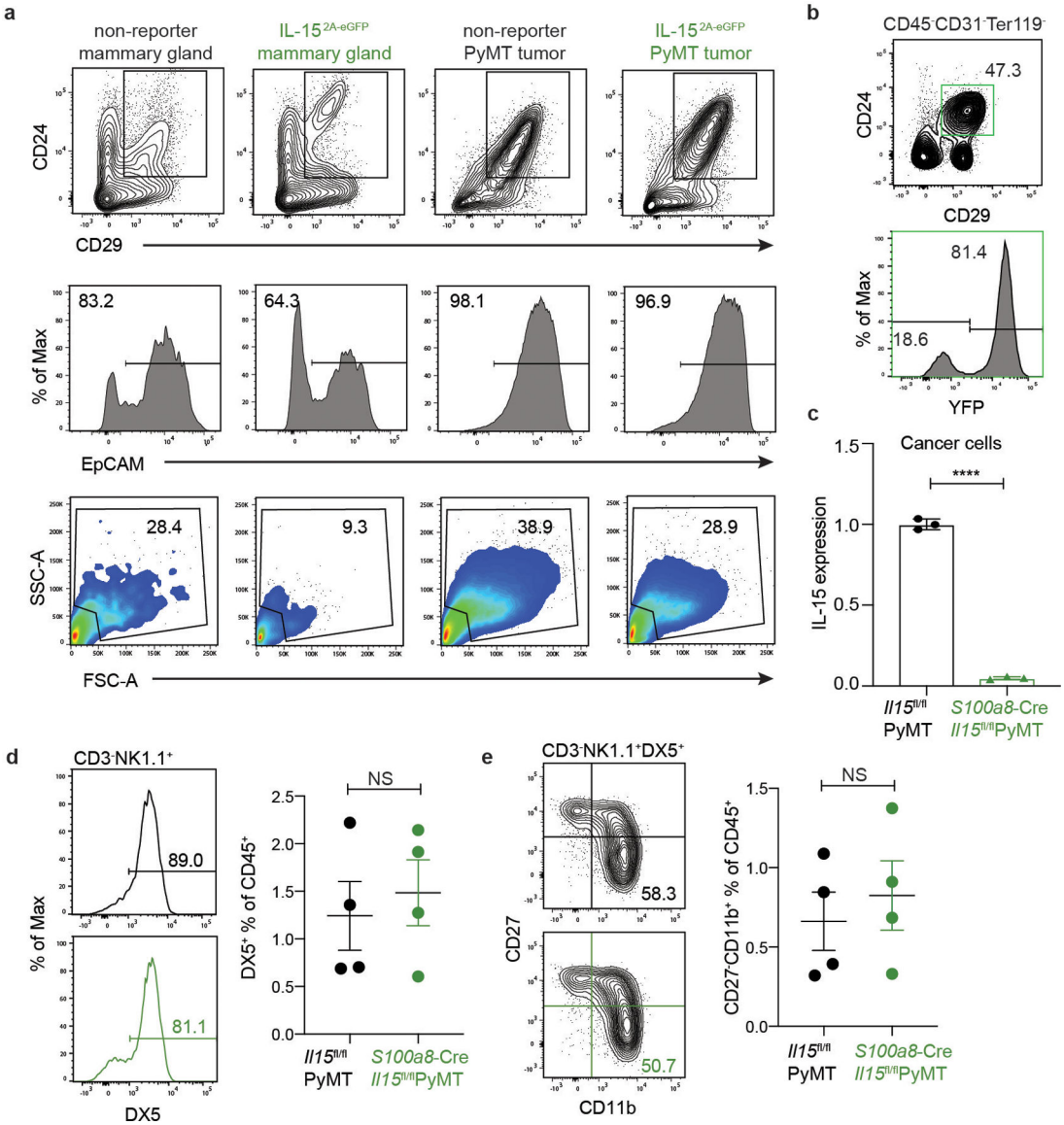


**Extended Data Fig. 9. *S100a8*-Cre targets cancer cells, and splenic NK cells are unaffected in *S100a8*-Cre*Il15*$^{fl/fl}$PyMT mice**

**a,** Gating strategy for determining eGFP expression in CD24$^{+}$CD29$^{+}$EpCAM$^{+}$ epithelial cells from non-reporter mammary gland, IL-15$^{2A\text{-}eGFP}$ mammary gland, PyMT tumors, and IL-15$^{2A\text{-}eGFP}$PyMT tumors. **b,** Gating strategy and YFP expression in CD24$^{+}$CD29$^{+}$ cancer cells from pooled tumors of a 20-week-old *S100a8*-Cre*Rosa26*$^{LSL\text{-}YFP}$PyMT mouse. **c,** qPCR analysis of *Il15* mRNA expression in sorted live CD45$^{-}$CD24$^{+}$CD29$^{+}$EpCAM$^{+}$ cancer cells from 20–24-week-old *Il15*$^{fl/fl}$PyMT (n = 3) or *S100a8*-Cre*Il15*$^{fl/fl}$PyMT mice (n = 3). **d,** (Left) Representative histograms of CD49b (DX5) expression among total CD3$^{-}$NK1.1$^{+}$ cells in spleens of the indicated mouse genotype. (Right) Percentage of DX5$^{+}$ NK cells quantified out of total splenic CD45$^{+}$ cells (n = 4 for each genotype). **e,** (Left) Representative plots of CD27 and CD11b expression among total CD3$^{-}$NK1.1$^{+}$DX5$^{+}$ cells in spleens of the indicated mouse genotype. (Right) Percentage of DX5$^{+}$CD11b$^{+}$CD27$^{-}$ cells quantified out of total splenic CD45$^{+}$ cells (n = 4 for each genotype). **c-e,** Each dot

represents an individual mouse. Data are pooled from 3 independent experiments. All error bars represent the mean ± SEM. Two-tailed unpaired t test was used for statistical analysis, NS = non-significant.

## Supplementary Material

Refer to Web version on PubMed Central for supplementary material.

## ACKNOWLEDGEMENTS:

The authors thank members of the Li laboratory for helpful discussions, Dr. Naikong Cheung for providing us with the human IL-15/IL-15Rα complex reagent, Dr. Morgan Huse for help with the single-cell killing microwell assay, and Dr. Katherine Hsu for providing us with the K562 cell line. This work was supported by National Institutes of Health: F31CA210332 (BGN), R01CA243904-01A1 (MOL), and P30 CA008748 (the Memorial Sloan Kettering Cancer Center Support Grant), Department of Defense: KC19008.e001 (MOL), Howard Hughes Medical Institute Faculty Scholar Award (MOL), Cancer Research Institute CLIP grant (MOL), Ludwig Center for Cancer Immunotherapy (MOL), and Functional Genomic Initiative (MOL).

## DATA MATERIALS AVAILABILITY:

All raw and processed single cell RNA have been deposited in GEO with accession ID GSE19978.

Source data for the following figures are available and listed in the Inventory of Supplemental Information: Fig. 5h–j, 6a, 7c,f; & Extended Data Fig. 6g–o, 7d–k, 9c–e. All other correspondence and requests for materials and/or data that support the findings of this study are available from and should be addressed to Dr. Ming O. Li (lim@mskcc.org).

## REFERENCES:

1. Burnet M Cancer: a biological approach. III. Viruses associated with neoplastic conditions. IV. Practical applications. Br Med J 1, 841–847 (1957). [PubMed: 13413231]
2. Schumacher TN & Schreiber RD Neoantigens in cancer immunotherapy. Science 348, 69–74 (2015). [PubMed: 25838375]
3. Sharma P & Allison JP Immune checkpoint targeting in cancer therapy: toward combination strategies with curative potential. Cell 161, 205–214 (2015). [PubMed: 25860605]
4. Motzer RJ, McHenry MB & Chen AC Immune Checkpoint Blockade in Advanced Renal-Cell Carcinoma. N Engl J Med 379, 92–93 (2018). [PubMed: 29972749]
5. Chiossone L, Dumas PY, Vienne M & Vivier E Natural killer cells and other innate lymphoid cells in cancer. Nat Rev Immunol 18, 671–688 (2018). [PubMed: 30209347]
6. Vivier E et al. Innate Lymphoid Cells: 10 Years On. Cell 174, 1054–1066 (2018). [PubMed: 30142344]
7. Dadi S et al. Cancer Immunosurveillance by Tissue-Resident Innate Lymphoid Cells and Innate-like T Cells. Cell 164, 365–377 (2016). [PubMed: 26806130]
8. Friedrich C et al. Effector differentiation downstream of lineage commitment in ILC1s is driven by Hobit across tissues. Nat Immunol 22, 1256–1267 (2021). [PubMed: 34462601]
9. Di Censo C et al. Granzyme A and CD160 expression delineates ILC1 with graded functions in the mouse liver. Eur J Immunol 51, 2568–2575 (2021). [PubMed: 34347289]
10. Bjorkstrom NK, Ljunggren HG & Michaelsson J Emerging insights into natural killer cells in human peripheral tissues. Nat Rev Immunol 16, 310–320 (2016). [PubMed: 27121652]
11. Cichocki F, Grzywacz B & Miller JS Human NK Cell Development: One Road or Many? Front Immunol 10, 2078 (2019). [PubMed: 31555287]

12. Mackay LK et al. Hobit and Blimp1 instruct a universal transcriptional program of tissue residency in lymphocytes. Science 352, 459–463 (2016). [PubMed: 27102484]
13. Collins PL et al. Gene Regulatory Programs Conferring Phenotypic Identities to Human NK Cells. Cell 176, 348–360 e312 (2019). [PubMed: 30595449]
14. Yomogida K et al. Hobit confers tissue-dependent programs to type 1 innate lymphoid cells. Proc Natl Acad Sci U S A 118, e2117965118 (2021). [PubMed: 34880136]
15. Diaz-Montero CM, Rini BI & Finke JH The immunology of renal cell carcinoma. Nat Rev Nephrol 16, 721–735 (2020). [PubMed: 32733094]
16. McGregor BA et al. Results of a Multicenter Phase II Study of Atezolizumab and Bevacizumab for Patients With Metastatic Renal Cell Carcinoma With Variant Histology and/or Sarcomatoid Features. J Clin Oncol 38, 63–70 (2020). [PubMed: 31721643]
17. Zhang N & Bevan MJ CD8(+) T cells: foot soldiers of the immune system. Immunity 35, 161–168 (2011). [PubMed: 21867926]
18. McFarland AP et al. Multi-tissue single-cell analysis deconstructs the complex programs of mouse natural killer and type 1 innate lymphoid cells in tissues and circulation. Immunity 54, 1320–1337 e1324 (2021). [PubMed: 33945787]
19. Hoffmann JC & Schon MP Integrin alphaE(CD103)beta7 in Epithelial Cancer. Cancers (Basel) 13, 6211 (2021). [PubMed: 34944831]
20. Borcherding N et al. Mapping the immune environment in clear cell renal carcinoma by single-cell genomics. Commun Biol 4, 122 (2021). [PubMed: 33504936]
21. Zhou Z et al. Granzyme A from cytotoxic lymphocytes cleaves GSDMB to trigger pyroptosis in target cells. Science 368, eaaz7548 (2020). [PubMed: 32299851]
22. Lieberman J Granzyme A activates another way to die. Immunol Rev 235, 93–104 (2010). [PubMed: 20536557]
23. Wagner JA et al. CD56bright NK cells exhibit potent antitumor responses following IL-15 priming. J Clin Invest 127, 4042–4058 (2017). [PubMed: 28972539]
24. Loibl S, Poortmans P, Morrow M, Denkert C & Curigliano G Breast cancer. Lancet 397, 1750–1769 (2021). [PubMed: 33812473]
25. Mamessier E et al. Human breast cancer cells enhance self tolerance by promoting evasion from NK cell antitumor immunity. J Clin Invest 121, 3609–3622 (2011). [PubMed: 21841316]
26. Zhang Y et al. Single-cell analyses reveal key immune cell subsets associated with response to PD-L1 blockade in triple-negative breast cancer. Cancer Cell 39, 1578–1593 e1578 (2021). [PubMed: 34653365]
27. Fluck MM & Schaffhausen BS Lessons in signaling and tumorigenesis from polyomavirus middle T antigen. Microbiol Mol Biol Rev 73, 542–563 (2009). [PubMed: 19721090]
28. Sosinowski T et al. CD8alpha+ dendritic cell trans presentation of IL-15 to naive CD8+ T cells produces antigen-inexperienced T cells in the periphery with memory phenotype and function. J Immunol 190, 1936–1947 (2013). [PubMed: 23355737]
29. Mortier E et al. Macrophage- and dendritic-cell-derived interleukin-15 receptor alpha supports homeostasis of distinct CD8+ T cell subsets. Immunity 31, 811–822 (2009). [PubMed: 19913445]
30. Franklin RA et al. The cellular and molecular origin of tumor-associated macrophages. Science 344, 921–925 (2014). [PubMed: 24812208]
31. Swonger JM, Liu JS, Ivey MJ & Tallquist MD Genetic tools for identifying and manipulating fibroblasts in the mouse. Differentiation 92, 66–83 (2016). [PubMed: 27342817]
32. Nixon BG et al. Cytotoxic granzyme C-expressing ILC1s contribute to antitumor immunity and neonatal autoimmunity. Sci Immunol 7, eabi8642 (2022). [PubMed: 35394814]
33. Eckl J et al. Transcript signature predicts tissue NK cell content and defines renal cell carcinoma subgroups independent of TNM staging. J Mol Med (Berl) 90, 55–66 (2012). [PubMed: 21870102]
34. Simoni Y et al. Human Innate Lymphoid Cell Subsets Possess Tissue-Type Based Heterogeneity in Phenotype and Frequency. Immunity 46, 148–161 (2017). [PubMed: 27986455]
35. Gao Y et al. Tumor immunoevasion by the conversion of effector NK cells into type 1 innate lymphoid cells. Nat Immunol 18, 1004–1015 (2017). [PubMed: 28759001]

36. Guan Y et al. Renal cell tumors convert natural killer cells to a proangiogenic phenotype. Oncotarget 11, 2571–2585 (2020). [PubMed: 32655841]
37. Burkett PR et al. Coordinate expression and trans presentation of interleukin (IL)-15Ralpha and IL-15 supports natural killer cell and memory CD8+ T cell homeostasis. J Exp Med 200, 825–834 (2004). [PubMed: 15452177]
38. Dubois S, Mariner J, Waldmann TA & Tagaya Y IL-15Ralpha recycles and presents IL-15 In trans to neighboring cells. Immunity 17, 537–547 (2002). [PubMed: 12433361]
39. Waldmann TA & Tagaya Y The multifaceted regulation of interleukin-15 expression and the role of this cytokine in NK cell differentiation and host response to intracellular pathogens. Annu Rev Immunol 17, 19–49 (1999). [PubMed: 10358752]
40. Mlecnik B et al. Functional network pipeline reveals genetic determinants associated with in situ lymphocyte proliferation and survival of cancer patients. Sci Transl Med 6, 228ra237 (2014).
41. Angelova M et al. Evolution of Metastases in Space and Time under Immune Selection. Cell 175, 751–765 e716 (2018). [PubMed: 30318143]
42. Freytag S, Tian L, Lonnstedt I, Ng M & Bahlo M Comparison of clustering tools in R for medium-sized 10x Genomics single-cell RNA-sequencing data. F1000Res 7, 1297 (2018). [PubMed: 30228881]
43. Haghverdi L, Lun ATL, Morgan MD & Marioni JC Batch effects in single-cell RNA-sequencing data are corrected by matching mutual nearest neighbors. Nat Biotechnol 36, 421–427 (2018). [PubMed: 29608177]
44. Lun AT, McCarthy DJ & Marioni JC A step-by-step workflow for low-level analysis of single-cell RNA-seq data with Bioconductor. F1000Res 5, 2122 (2016). [PubMed: 27909575]
45. Levine JH et al. Data-Driven Phenotypic Dissection of AML Reveals Progenitor-like Cells that Correlate with Prognosis. Cell 162, 184–197 (2015). [PubMed: 26095251]
46. Xu C & Su Z Identification of cell types from single-cell transcriptomes using a novel clustering method. Bioinformatics 31, 1974–1980 (2015). [PubMed: 25805722]
47. Liu M et al. TGF-beta suppresses type 2 immunity to cancer. Nature 587, 115–120 (2020). [PubMed: 33087928]
48. Yuan TL & Cantley LC PI3K pathway alterations in cancer: variations on a theme. Oncogene 27, 5497–5510 (2008). [PubMed: 18794884]

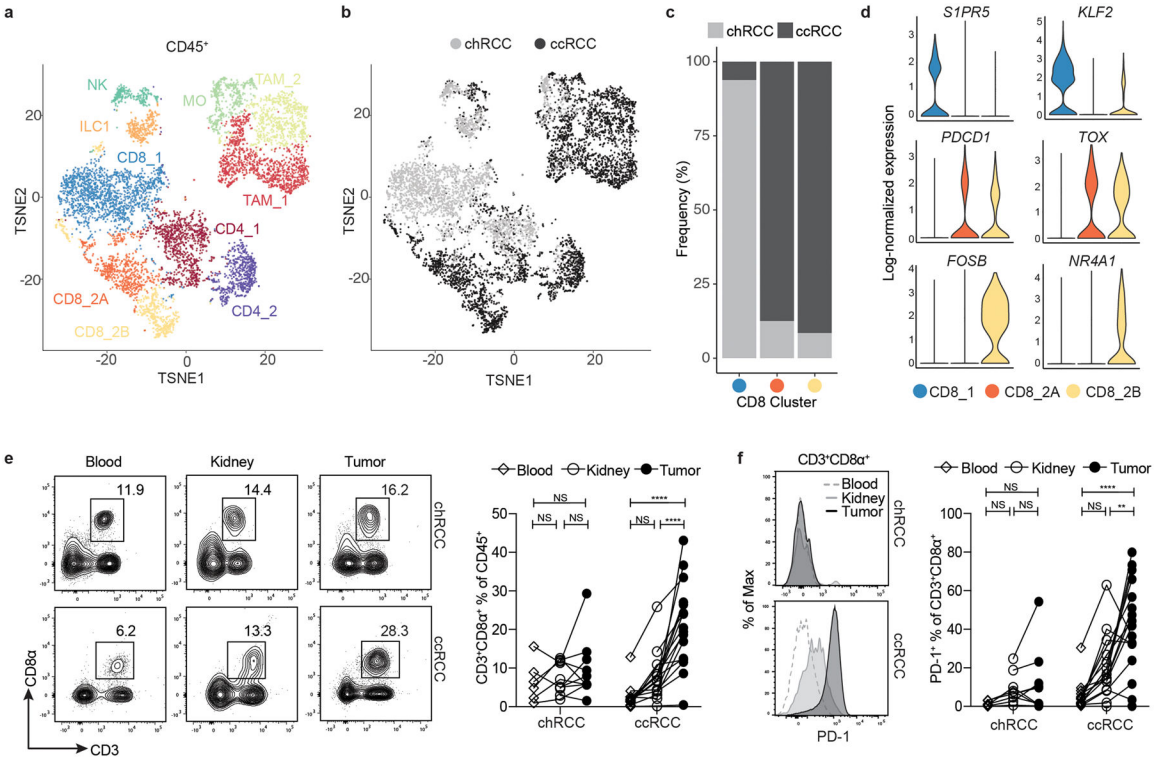


**Figure 1. chRCC and ccRCC tumor exhibit differential immune cell infiltration and CD8 T cell phenotypes**

**a,** t-distributed Stochastic Neighbor Embedding (tSNE) embedding of transcriptional profiles from leukocytes isolated from one chromophobe renal cell carcinoma (chRCC) tumor and one clear cell RCC (ccRCC) tumor. Each dot represents a single $CD45^+$ cell, and colors represent clusters denoted by cell type inferred from lineage markers and differential gene expression. **b,** tSNE plot as in **a**, colored by histology (chromophobe or clear cell). **c,** For each CD8 cluster, the frequency out of all $CD8\alpha^+$ clusters at which it was found in chRCC (n = 1) and ccRCC (n = 1) tumors. **d,** Violin plots showing log-normalized expression of selected differentially expressed genes among three CD8 clusters. **e,** Representative plots of flow cytometric analysis of the percentage of $CD3^+CD8\alpha^+$ T cells out of the lymphocyte gate ($CD45^+SSC^{Low}$) in blood, adjacent normal kidney, and tumor samples from one patient of the indicated histology. Quantification is $CD3^+CD8\alpha^+$ T cells out of total $CD45^+$ cells. **f,** Representative histograms of PD-1 expression in $CD3^+CD8\alpha^+$ T cells from blood, adjacent normal kidney, and tumor tissues from a single patient of the indicated histology. Quantification of flow cytometric analysis of percentage of $PD\text{-}1^+CD3^+CD8\alpha^+$ T cells in blood, adjacent normal kidney, and tumor samples from the indicated histology. **e, f,** Each pair of symbols connected by a line denotes an individual patient [chRCC blood n = 6 (**e** and **f**), kidney n = 9 (**e**) and 10 (**f**), tumor n = 9 (**e**) and 10 (**f**); ccRCC blood n = 14, kidney n = 15, tumor n = 16]. One-way ANOVA with Tukey's multiple comparison test was used for statistical analysis, NS = non-significant, $^{**}p < 0.01$, $^{****}p < 0.0001$.

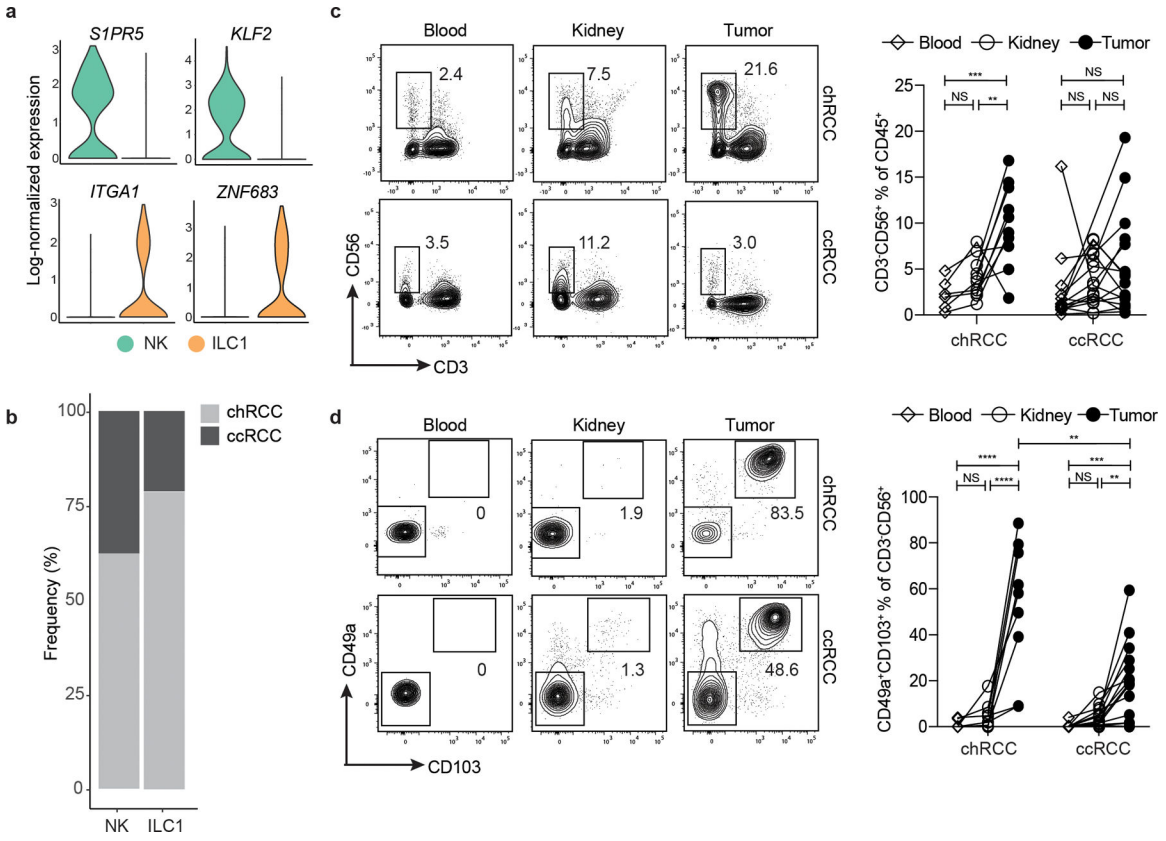


**Figure 2. chRCC tumors are highly infiltrated by CD56$^{+}$CD49a$^{+}$CD103$^{+}$ ILC1s**

**a,** Violin plots showing log-normalized expression of differentially expressed genes between NK and ILC1 clusters. **b,** For each innate lymphocyte (*KLRB1*$^{+}$) cluster, the frequency out of all *KLRB1*$^{+}$ clusters at which it was found in chRCC (n = 1) and ccRCC (n = 1) tumors. **c,** Representative plots of flow cytometric analysis of the percentage of CD3$^{-}$CD56$^{+}$ innate lymphocytes out of the lymphocyte gate (CD45$^{+}$SSC$^{Low}$) in blood, adjacent normal kidney, and tumor samples from one patient of the indicated histology. Quantification is CD3$^{-}$CD56$^{+}$ innate lymphocytes out of total CD45$^{+}$ cells. **d,** Representative plots of flow cytometric analysis of the percentage of CD49a$^{+}$CD103$^{+}$ ILC1s out of the innate lymphocyte gate (CD3$^{-}$CD56$^{+}$) in blood, adjacent normal kidney, and tumor samples from one patient of the indicated histology. Quantification is CD49a$^{+}$CD103$^{+}$ ILC1s out of CD3$^{-}$CD56$^{+}$ innate lymphocytes. **c, d,** Each pair of symbols connected by a line denotes an individual patient [chRCC blood n = 6 (**c** and **d**), kidney n = 10 (**c**) and 9 (**d**), tumor n = 10 (**c**) and 9 (**d**)), ccRCC blood n = 14, kidney n = 15, tumor n = 16]. One-way ANOVA with Tukey's multiple comparison test was used for statistical analysis. Two-tailed unpaired t test was used to analyze significance of ILC1 abundance in chRCC versus ccRCC tumors. NS = non-significant, **p < 0.01, ***p < 0.001, ****p < 0.0001.

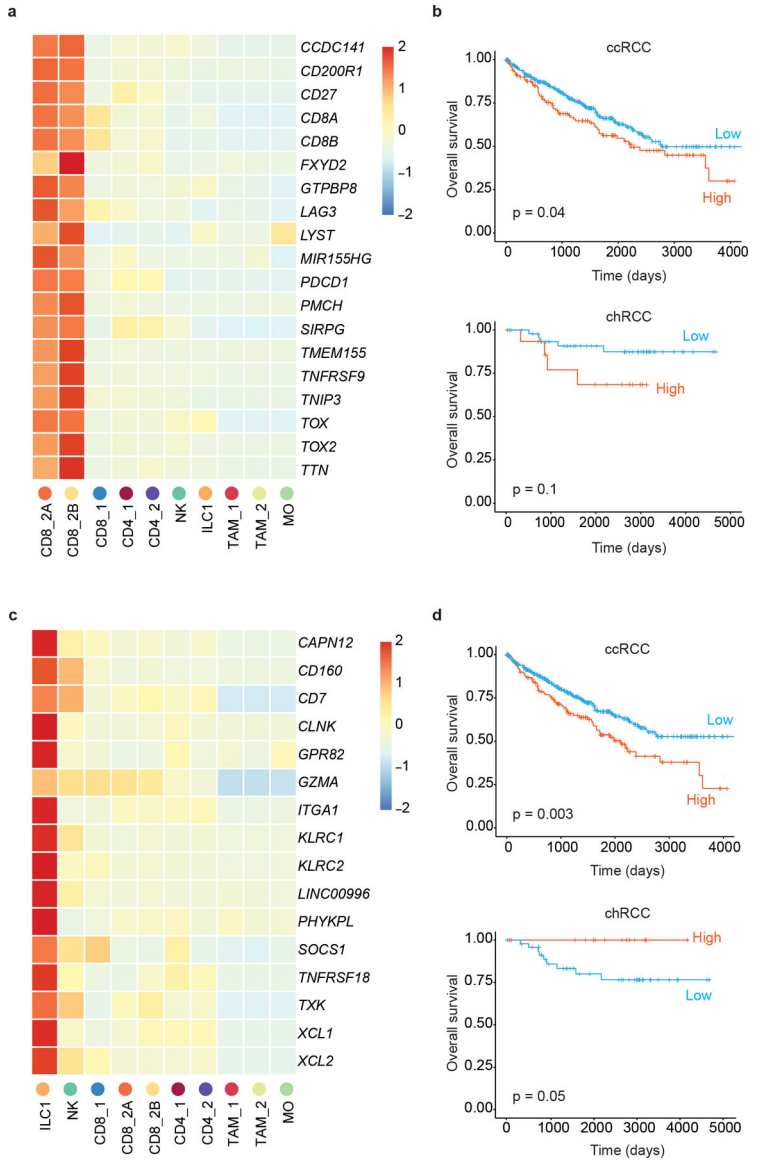


**Figure 3. High expression of the ILC1 signature predicts better survival of chRCC patients**

**a,** Heatmap showing enrichment of the CD8_2 signature genes in the indicated clusters. **b,** Survival analysis demonstrating association of the CD8_2 signature across the TCGA ccRCC (top, 535 patients) and chRCC (bottom, 66 patients) cohorts. **c,** Heatmap showing enrichment of the ILC1 signature genes in the indicated clusters. **d,** Survival analysis demonstrating association of the ILC1 signature across the TCGA ccRCC (top, 535 patients) and chRCC (bottom, 66 patients) cohorts. **b, d,** High represents the top quartile of the distribution of signature scores, low represents the bottom 3 quartiles. Statistical p values calculated using a Cox regression and log-rank test.

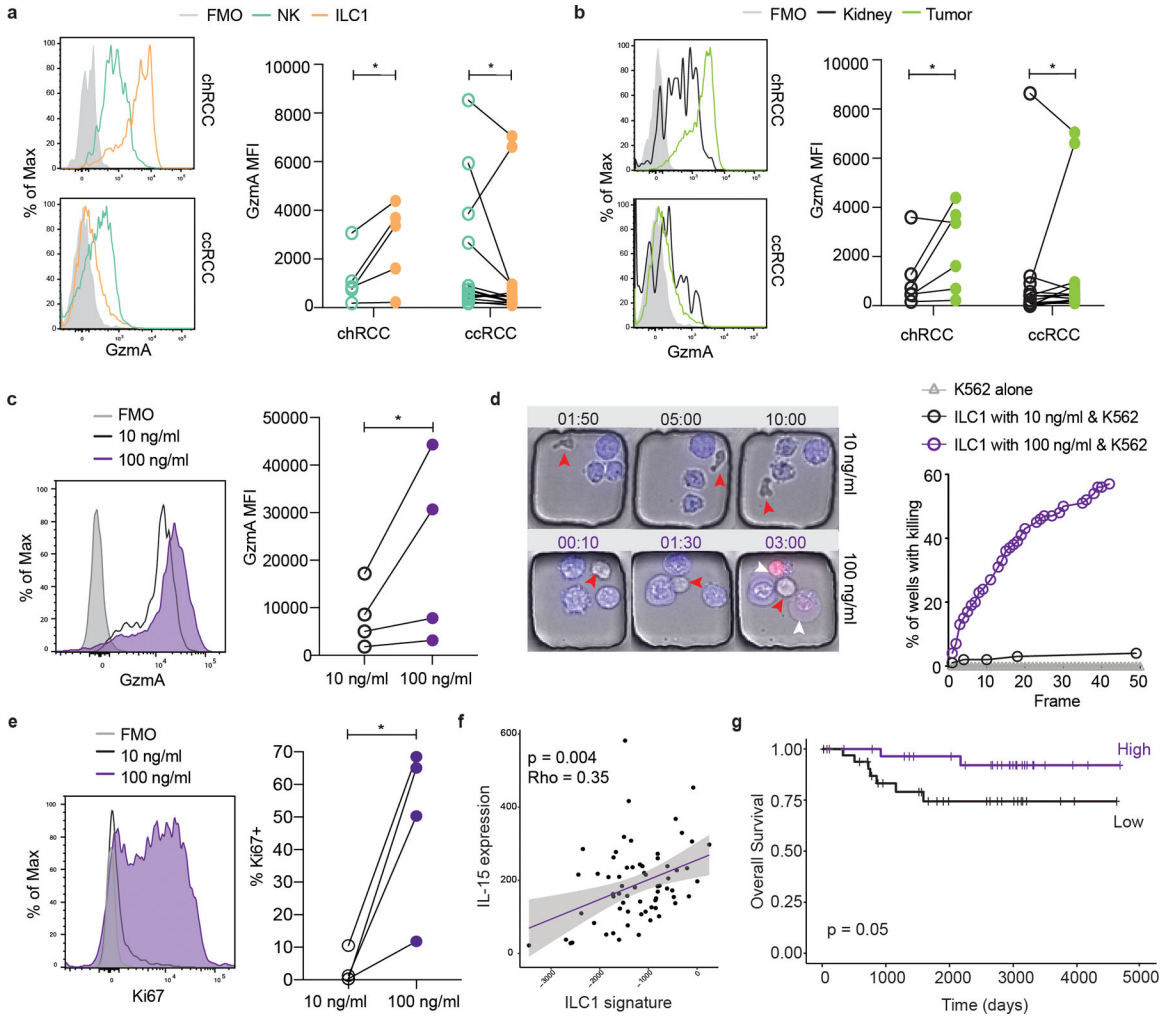


**Figure 4. IL-15 governs the cytolytic effector function of ILC1s in RCC**

**a,** Representative plots and quantification of granzyme A (GzmA) mean fluorescence intensity (MFI) in CD49a$^{-}$CD103$^{-}$ NK cells and CD49a$^{+}$CD103$^{+}$ ILC1s from chRCC (n = 5) and ccRCC (n = 14) tumors. Each pair of symbols connected by a line denotes an individual patient. FMO = fluorescence minus one control. **b,** Representative plots and quantification of GzmA expression in ILC1s in adjacent normal kidney and tumor from chRCC (n = 6) and ccRCC (n = 14) patients. **c,** Representative plots and quantification of GzmA expression in RCC tumor ILC1s (n = 4) cultured with the indicated concentrations of IL-15/IL-15Rα complex. **d,** Representative still images and quantification of cytolytic activities of ILC1s cultured with the indicated concentrations of IL-15/IL-15Rα complex. Times are in format of hour:minute. Blue cells are cell trace violet (CTV)-stained K562 target cells. Red arrows indicate ILC1s and white arrows indicate dead K562 target cells. Plot is representative of 3 independent experiments using cells isolated from 3 different RCC patients. **e,** Representative plots and quantification of Ki67 expression in RCC tumor ILC1s (n = 4) cultured with the indicated concentrations of IL-15/IL-15Rα complex. **f,** Correlation between level of IL-15 expression and ILC1 signature in chRCC cases from the TCGA database. Statistical analyses calculated using Spearman's correlation. Error bands represent

the 95% confidence interval. **g,** Association of IL-15 expression and overall survival across the TCGA chRCC cohort. High represents the top quartile and low represents the bottom 3 quartiles of IL-15 expression level. P value calculated using a Cox regression and log-rank test. **a, b, c,** Paired ratio t test was used for statistical analysis. *p < 0.05. **e,** Two-tailed unpaired t test was used for statistical analysis, *p < 0.05.

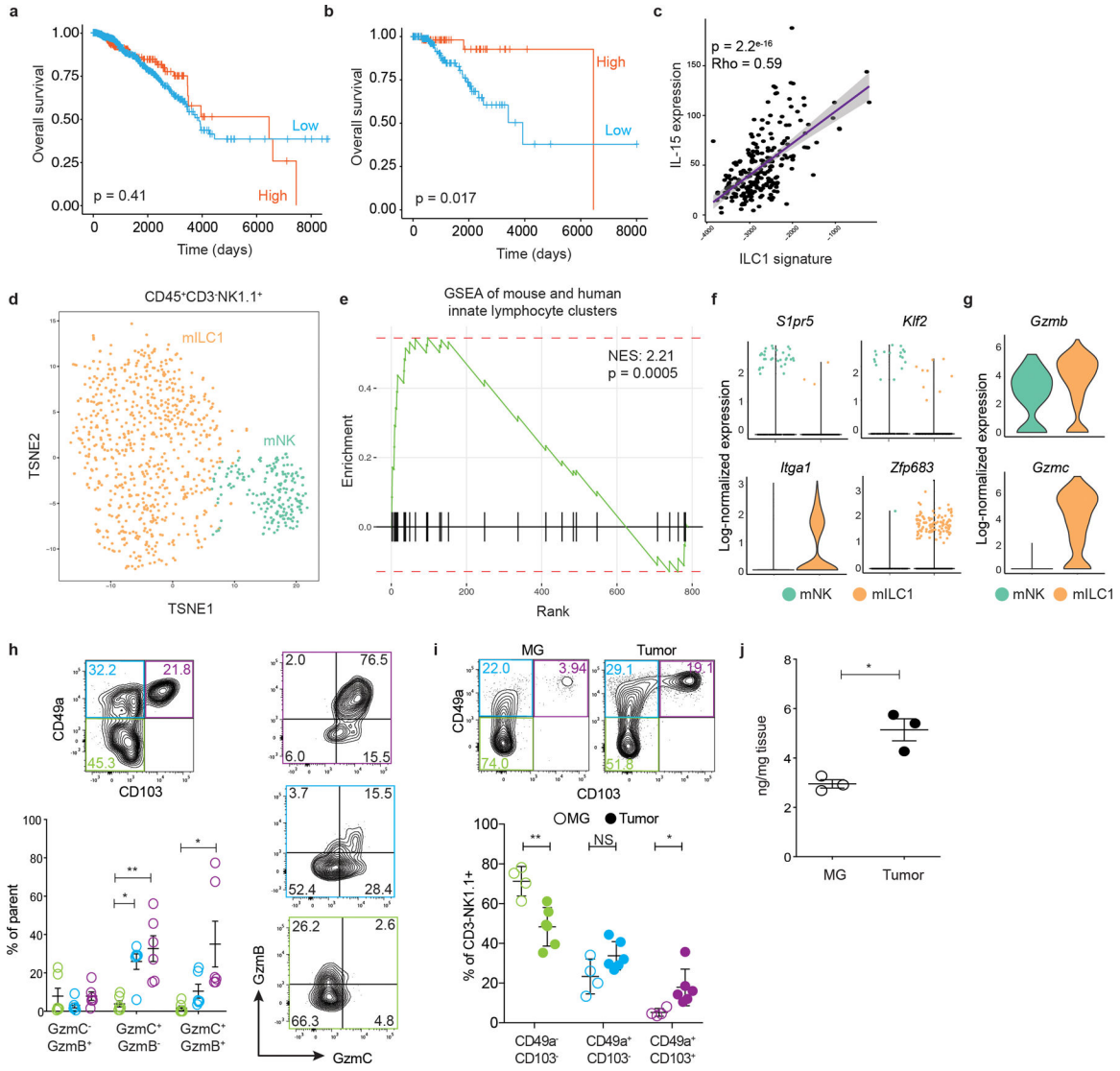


**Figure 5. ILC1s are induced in human and murine breast cancers in association with IL-15 expression in tumor**

**a, b,** Survival analysis of ILC1 signature across the TCGA BRCA (1102 patients) cohort (**a**) and a subset of BRCA (231 patients) with hotspot activating mutations (p.H1047R, p.E545K, p.E542K) in *PIK3CA* (**b**). High represents the top quartile of the distribution of signature scores, low represents bottom 3 quartiles. Statistical p values calculated using Cox regression and log-rank test. **c,** Correlation between IL-15 expression and ILC1 signature in a cohort of BRCA patients with hotspot activating mutations in *PIK3CA* (231 patients). Statistical analyses calculated using Spearman's correlation. Error bands represent the 95% confidence interval. **d,** tSNE embedding of transcriptional profiles from pooled tumors of a PyMT mouse. Each dot represents a single $CD3^{-}NK1.1^{+}$ cell, colors represent murine ILC1 (mILC1) and murine NK (mNK) clusters. **e,** GSEA of the list of DEGs between clusters mNK and mILC1 against the list of DEGs between human clusters NK and ILC1. P-value calculated using GSEA pre-ranked analysis with log fold changes as input. **f, g,** Violin plots showing log-normalized expression of selected differentially expressed

genes between mNK and mILC1 clusters. **h,** A representative plot of CD49a and CD103 expression in $CD3^{-}NK1.1^{+}$ innate lymphocytes with representative plots and quantification of granzyme B (GzmB) and granzyme C (GzmC) expression within the $CD49a^{-}CD103^{-}$, $CD49a^{+}CD103^{-}$, and $CD49a^{+}CD103^{+}$ subsets. Data are pooled from 3 or more independent experiments. **i,** Representative plots and quantification of $CD3^{-}NK1.1^{+}$ innate lymphocyte subsets in healthy mammary glands (MG) and PyMT mammary tumors. Data are pooled from 3 or more independent experiments (MG n = 4, tumor n = 5–6). **g,** IL-15 ELISA on pooled MG and PyMT tumors. IL-15 quantity in ng was calculated for 1 mg of tissue. **h, i,** All error bars represent the mean ± SEM. One-way ANOVA with Tukey's multiple comparison test was used for statistical analysis. **j,** Data representative of 3 separate experiments. Error bars represent the mean ± SEM. Two-tailed unpaired t test was used for statistical analysis. NS = non-significant, *$p < 0.05$, **$p < 0.01$.

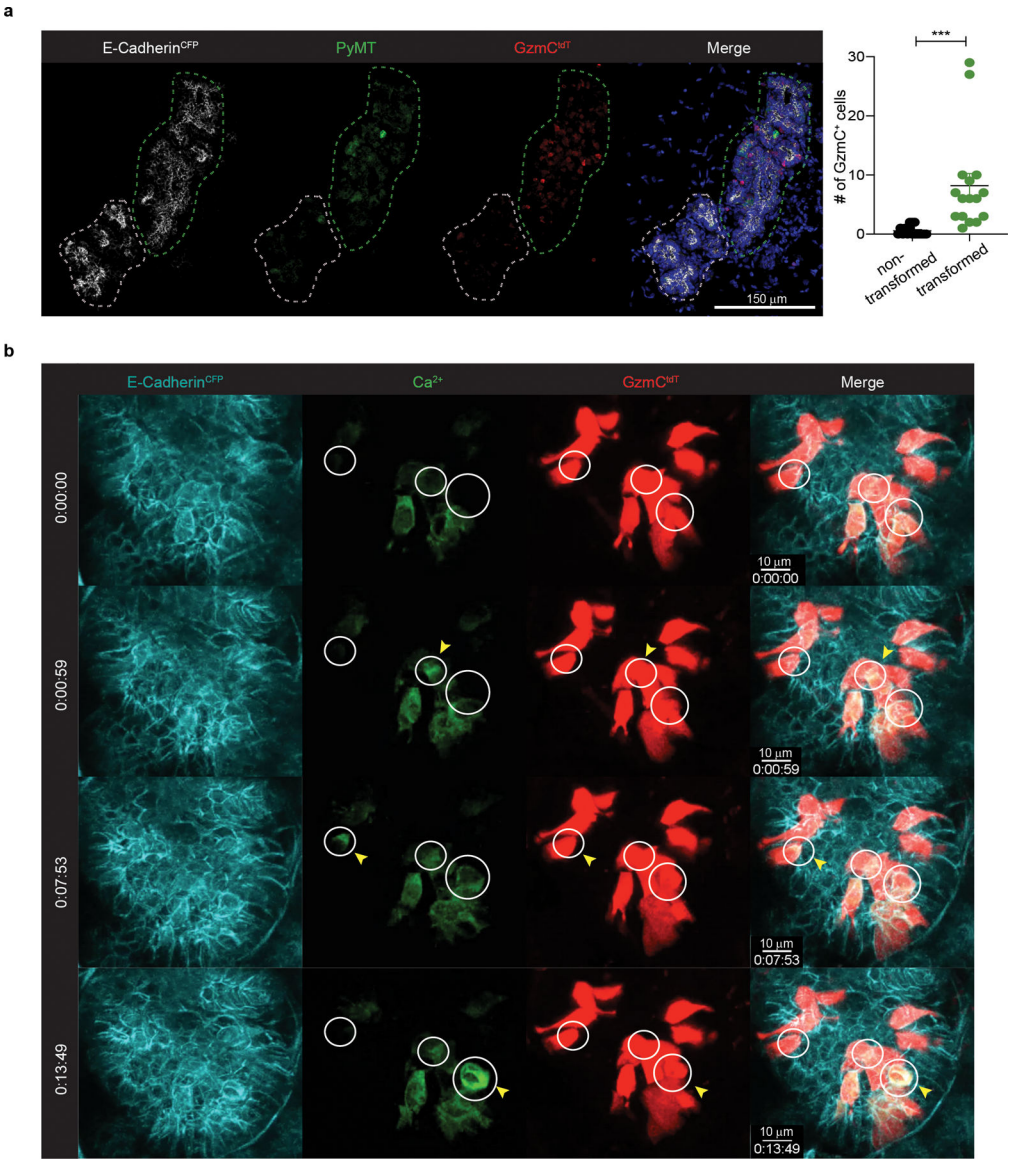


**Figure 6. ILC1s expand in transformed tissue where they are stationary but active**

**a,** Representative immunofluorescence images of E-cadherin$^{CFP}$ (white), PyMT (green), GzmC$^{tdT}$ (red), and DAPI (blue) from a tumor section of a 13-week-old *Gzmc*$^{tdT\text{-}T2A\text{-}iCre}$*Cdh1*$^{mCFP}$PyMT mouse. Scale bar, 150 μM. Green outline denotes transformed (PyMT$^{+}$) area and white outline denotes non-transformed (PyMT$^{-}$) area. Quantification is of total number of individual GzmC$^{tdT}$-positive cells in non-transformed or transformed areas, taken from tumor sections of two individual mice, each with 4–5 fields of view and a range of 1–8 distinct regions of non-transformed or transformed areas. Each dot represents discrete, individual E-Cadherin$^{+}$ areas. Error bars represent the mean ± SEM. Two-tailed unpaired t test was used for statistical analysis, ***$p < 0.001$. **b,** Still images of live imaging time lapse of a mammary gland from a 13-week-old PyMT mouse with E-cadherin$^{CFP}$ (teal), $Ca^{2+}$ (green), and GzmC$^{tdT}$ (red). Data shown is representative of two

independent experiments. Scale bar, 10 μM. Circles denote cells in which we observe a calcium flux, indicated by a yellow arrow.

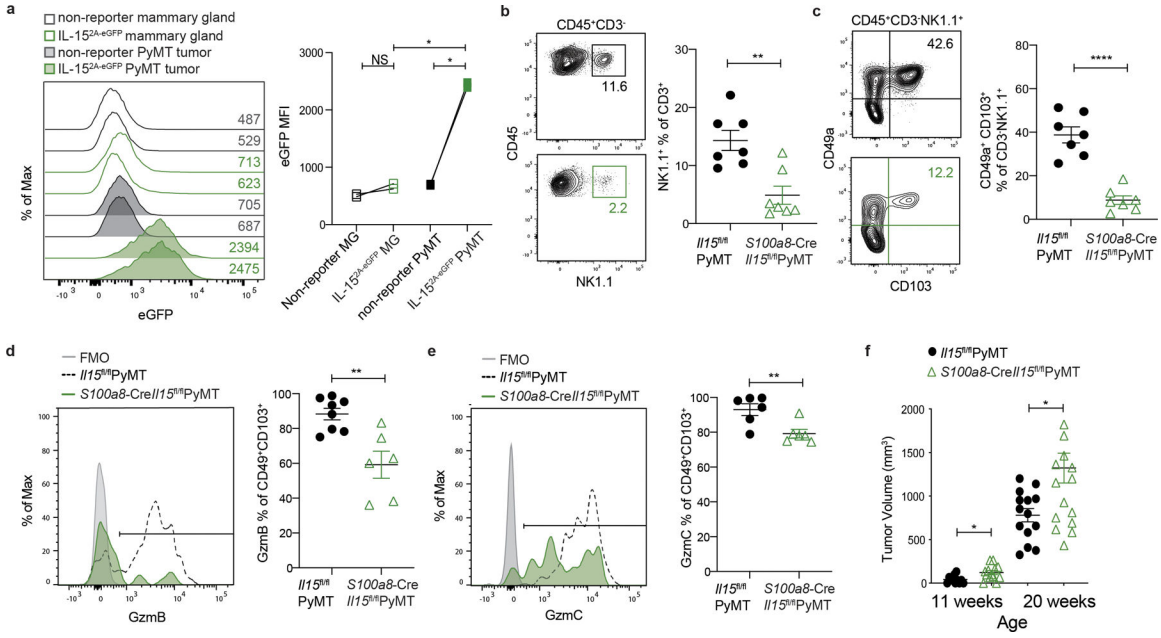


**Figure 7. Cancer cell-expressed IL-15 promotes ILC1 responses in tumor**

**a,** Flow cytometric analysis of eGFP expression in $CD24^{+}CD29^{+}EpCAM^{+}$ epithelial cells from mammary tissues of 20-week-old IL-$15^{2a\text{-}eGFP}$PyMT (green solid), IL-$15^{2a\text{-}eGFP}$ (green empty), PyMT (gray filled), or control mouse (gray empty) (n = 2 mice for each group). Numbers represent mean fluorescence intensity (MFI). Plot is representative of 2 independent experiments. Paired ratio t tests were used for statistical analysis, NS = non-significant, *$p < 0.05$. **b,** Representative plots and quantification of percentage of $NK1.1^{+}$ cells out of total $CD45^{+}CD3^{-}$ cells isolated from pooled tumors of 20–24-week-old *Il15*$^{fl/fl}$PyMT (n = 6) or *S100a8*-Cre*Il15*$^{fl/fl}$PyMT (n = 7) mice. **c,** Representative plots and quantification of percentage of $CD49a^{+}CD103^{+}$ ILC1s out of total $CD45^{+}CD3^{-}NK1.1^{+}$ cells isolated from pooled tumors of 20–24-week-old *Il15*$^{fl/fl}$PyMT (n = 6) or *S100a8*-Cre*Il15*$^{fl/fl}$PyMT mice (n = 7). **d,** A representative histogram and quantification of granzyme B (GzmB) expression in $CD49a^{+}CD103^{+}$ ILC1s from pooled tumors of 20–24-week-old *Il15*$^{fl/fl}$PyMT (n = 8) or *S100a8*-Cre*Il15*$^{fl/fl}$PyMT (n = 6) mice. **e,** A representative histogram and quantification of granzyme C (GzmC) expression in $CD49a^{+}CD103^{+}$ ILC1s from pooled tumors of 20–24-week-old *Il15*$^{fl/fl}$PyMT (n = 6) or *S100a8*-Cre*Il15*$^{fl/fl}$PyMT (n = 6) mice. **f,** Total tumor burden of *Il15*$^{fl/fl}$PyMT (11 weeks n = 11, 20 weeks n = 14) and *S100a8*-Cre*Il15*$^{fl/fl}$PyMT (11 weeks n = 13, 20 weeks n = 14) mice monitored between 11 and 20 weeks of age. Error bars represent the mean ± SEM. Two-tailed unpaired t test was used for statistical analyses, *$p < 0.05$. **b-e,** Data are pooled from 3 or more independent experiments. Each dot represents an individual mouse. All error bars represent the mean ± SEM. Two-tailed unpaired t test was used for all statistical analyses, **$p < 0.01$, ****$p < 0.0001$.